Extracting Sea Ice Topographic Features From Triangulated Surface Models

Yunting Song, Leila De Floriani, *Fellow, IEEE*, Kyle Duncan, and Sinéad Louise Farrell

***Abstract*—Pressure ridges are the dominant topographic features of sea ice, playing a critical role in momentum transfer between the atmosphere and ocean. However, characterizing their 3-D morphology remains a challenge. Traditional methods, applied to linear profile data from laser altimeters, cannot extract 2-D features, specifically the horizontal orientation, extent, and connectivity of deformed ice. To address this gap, this article introduces a novel strategy to extract pressure ridges directly from altimeter swath data by utilizing triangulated irregular networks (TINs) and surface topology. Unlike raster grid-based models, TIN-based surface models do not require interpolation, thereby preserving the original point dataset and effectively retaining line features, which are essential for ridge extraction. Our algorithm integrates discrete Morse theory with surface roughness constraints to identify ridge structure lines from level sea ice. In addition, we discuss how to address data dropout issues in the generation of a TIN-based surface model, which prevents the correct extraction of ridge structures. The point cloud used in this study is high-resolution swath data from the NASA Operation IceBridge (OIB) Airborne Topographic Mapper (ATM). The validation against two independent datasets, the linear profile data collected by Ice, Cloud, and land Elevation Satellite (ICESat-2) and optical imagery captured during the OIB campaign, demonstrates that the proposed ridge extraction method can effectively detect ridge lines from TIN-based models. Such ridge features can provide more information about sea ice ridges, such as length, average height, and orientation, which is not possible when using linear profiles or gridded surface models.**

***Index Terms*—Altimetry, sea ice, terrain analysis, topological methods, triangular irregular networks (TINs).**

I. Introduction

UNDERSTANDING sea ice topography is crucial to identify the drivers of sea ice variability and to quantify the impact of roughness on various sea ice processes. Rough topographic features on the sea ice surface, such as ridge sails, hummocks, sastrugi, snow dunes, melt ponds, and leads, influence heat and momentum fluxes between the polar atmosphere and ocean [1], particularly atmospheric drag [2], [3]. In particular, pressure ridges, formed by collisions between sea ice floes due to atmosphere and/or ocean forcing, act as the primary contributors to sea ice roughness. Mapping ridged ice is essential for sea ice navigability analysis [4], atmosphere-ice-ocean momentum transfer modeling [1], and airborne electromagnetic sea ice thickness measurements [5]. Ridge sail density has also proven to be a good indicator of the degree of ice deformation [6]. The geometry of ridge sails (heights and widths), as well as pressure ridge density, are necessary inputs for atmospheric drag parameterizations [3]. Moreover, recent rapid declines in the extent and thickness of the Arctic sea ice cover [7], [8] making timely measurements and analysis of topographic features on the sea ice surface even more important.

Despite their importance, accurately characterizing ridge geometry remains a challenge. Satellite laser altimeters, deployed on the Ice, Cloud, and land Elevation Satellite (ICESat) and ICESat-2 [9], provide sea ice elevation measurements from which ridge peaks can be detected [10]. However, these observations are inherently limited to one dimension and cannot capture the full 3-D morphology or orientation of ridge structures due to the large spacing (3 km) between ground tracks. To overcome this, our work leverages high-resolution airborne swath-mapping laser altimetry with the Airborne Topographic Mapper (ATM) [11]. The ATM swath, from a nominal flight altitude, reached widths of 200–300 m across the flight track, offering us the opportunity to extract 2-D features from sea ice surfaces that are otherwise difficult to obtain from linear profiles [12].

However, existing methods for analyzing sea ice topography from such swath data usually require conversion of point cloud data into raster grids [12], [13] first. This process introduces sampling loss and interpolation errors, making it impossible to use the full information from the original swath data. To address these issues, we propose a new method to extract the surface expression of pressure ridges (ridge sail) based on triangulated irregular networks (TINs). Unlike gridded models, a TIN can be generated directly from point cloud data without resampling, and thus, a TIN-based surface model can maintain all information derived from the elevation measurements. In addition, TINs can include accurate line features and boundaries of regional features, which are beneficial in accurate ridge structure extractions. In the sea ice field, triangle meshes have

Received 1 April 2025; revised 14 September 2025 and 1 February 2026; accepted 25 March 2026. Date of publication 5 May 2026; date of current version 27 May 2026. The work of Yunting Song and Leila De Floriani was supported by U.S. National Science Foundation under Grant IIS-1910766 and Grant IIS-2114451. The work of Kyle Duncan and Sinéad Louise Farrell was supported by NASA Earth Sciences Division Cryosphere Program under Grant 80NSSC24K1450 and Grant 80NSSC20K0966. *(Corresponding author: Yunting Song.)*

Yunting Song, Leila De Floriani, and Sinéad Louise Farrell are with the Department of Geographical Sciences, University of Maryland, College Park, MD 20740 USA (e-mail: ytsong@umd.edu; deflo@umd.edu; sineadf@umd.edu).

Kyle Duncan is with the Earth System Science Interdisciplinary Center, University of Maryland, College Park, MD 20740 USA (e-mail: kduncan@umd.edu).

This article has supplementary downloadable material available at https://doi.org/10.1109/TGRS.2026.3690366, provided by the authors.

Digital Object Identifier 10.1109/TGRS.2026.3690366

been used in simulation models [5], [14], and mass change evaluation [15], but they have not been employed to extract topographic features on sea ice.

The primary contribution of this study is a novel, topology-based method for extracting 3-D pressure ridge structures from airborne LiDAR swath data. We utilize surface topology, defined via discrete Morse theory [16], to extract the structural expressions of sea ice ridges from TINs. This includes the line along the ridge crest (i.e., the raised part of a ridge) and the steepest lines extending down from the ridge peak to the level ice surface. Unlike traditional profile-based methods, our approach identifies the full, multidirectional geometry of ridge structures, offering a more complete characterization.

In addition, we present three methodological contributions that have been applied to ensure the fidelity and robustness of the extraction process as follows.

1) A robust strategy to construct a TIN-based representation of the sea ice surface. It involves mesh generation through Delaunay triangulation [17] and artifact removal through the α-shape method [18]. This ensures that the surface topology is calculated from a valid sea ice surface, avoiding false boundaries introduced by data dropouts or triangulation artifacts (see Section IV-B).
2) A roughness-based postprocessing filter. We utilize local surface roughness calculated on the TIN-based model as a metric to differentiate topographic features from level sea ice. This allows us to effectively trim the ridge structures that would otherwise extend into flat regions (see Section IV-C).
3) Parameter calibration with discussion and multisource validation. We conduct a set of systematic experiments to select parameters in this workflow, and discuss the rationale behind their selection (see Section V). Moreover, we validate the extracted features against coincident ICESat-2 [9] elevation data and optical imagery [19] in Section VI.

The remainder of this article is organized as follows. Section II reviews related work on sea ice topography study with a focus on pressure ridge extraction methods. Section III introduces the datasets we used in this work. Section IV details the proposed method for ridge extraction, and Section V discusses how we calibrate the values of parameters used by this method. The results of sea ice surface model generation and ridge extraction are presented in Section VI. Section VII discusses the advantages of the proposed TIN-based framework for sea ice topographic analysis and the broader implications of our results.

II. Related Work

In this section, we review research related to this work from two aspects. Section II-A reviews major data sources for sea ice topography analysis, and Section II-B covers recent work on sea ice ridge extraction.

A. Remote Sensing of Sea Ice Topography

Recent advances in remote sensing techniques [20], [21], like satellite laser and radar altimetry and synthetic aperture radar (SAR), provide opportunities for regular large-scale observations of sea ice surface conditions [22]. From 2003 to 2009, the ICESat mission collected surface elevation profiles with single-beam waveform LiDAR [23], allowing topographic analysis, such as sea ice freeboard calculation [24]. Its successor, ICESat-2 [9] has been collecting continual measurements over both polar regions with the advanced topographic laser altimeter system (ATLAS) [21] since its launch in 2018. ATLAS produces three beam pairs, each consisting of one strong and one weak beam, with 3-km spacing between pairs and 90-m spacing within each pair [9]. These large-scale elevation measurements are vital for characterizing the sea ice surface. Recent research [25] has demonstrated the possibility of extracting detailed topographic features, including surface roughness, pressure ridges, melt ponds, ice floes, and leads from ICESat-2 elevation data. However, the topographic analysis on both systems relies on along-track elevation profiles and is limited to one dimension, leaving the morphology between tracks unmeasured.

To resolve 2-D sea ice topographic features, airborne laser scanners such as the ATM are essential. Unlike satellite profilers, the ATM employs a conically scanning laser that measures a swath of topography [11]. This swath coverage is critical for identifying the orientation and connectivity of pressure ridges, which is impossible with 1-D profiles alone. From 2009 to 2019, the NASA Operation IceBridge (OIB) campaign [26] performed annual surveys of the Arctic region with a large set of instruments, including laser altimeters, a snow radar, a radar altimeter, and an optical camera.

In addition to laser altimetry, recent studies also demonstrate the possibility of using SAR interferometry for topographic mapping. For instance, research utilizing the interferometric TanDEM-X data has demonstrated the feasibility of retrieving 2-D sea ice topographic heights from single-pass interferometric SAR (InSAR) data [27], [28]. More recently, dual-polarimetric approaches have been proposed to mitigate signal penetration biases in these measurements and to improve the accuracy of generated elevation models [29]. While InSAR data offers improvements in spatial coverage, it often lacks the vertical precision and spatial resolution of airborne LiDAR, particularly for resolving the small-scale ridge features.

B. Pressure Ridge Extraction Methods

Historically, most large-scale studies on sea ice pressure ridges rely on images [10], [30], [31], [32] or on laser altimetry data [2], [12], [25], [33], [34]. Edge detection and object detection are the main approaches used in image-based studies to identify ridges. Miao et al. [30] detect the shadows from the aerial images to derive the locations and heights of ridges. A similar method is used by Duncan et al. [10], [32] to derive ridge sail heights from OIB digital mapping system (DMS) images, and the results are validated with OIB ATM data. Linow and Dierking [31] apply edge detection to sea ice images to extract linear kinematic features (LKFs), which comprise leads, cracks, and pressure ridges. There is no elevation information in the images employed by those methods, and thus, the ridge height can only be inferred [32] but not directly measured.

Direct measurements of ridge sail heights are usually obtained in situ during field work, from airborne laser altimeters [33], [35], [36], or from satellite laser altimeters [34]. Most existing studies use 1-D laser altimetry profiles and identify ridges from profiles as local maxima along the profile [2], [25], [33], [34]. However, profile-based ridge extraction is limited to one direction and can only capture ridges intersecting the survey track. Besides, they cannot be used to extract complex, multidirectional ridges. With laser altimetry profile data, a comprehensive view of ridges in a region can only be obtained by extrapolating from the 1-D result. Such an extrapolation relies on the assumption that the 2-D distribution of ridges has the same pattern as the distribution along the ground track, which may not always be the case, particularly in regions of heavy deformation close to the coast.

Compared to laser altimeter profilers, LiDAR swaths offer more comprehensive coverage, allowing for the extraction of two- or 3-D features on sea ice, including ridges. One recent study that leverages the 3-D coverage of LiDAR data to extract surface roughness characteristics was conducted by Petty et al. [12]. They grid OIB ATM points into a 2-m resolution gridded DEM and extract peaks as local maxima within the grid. A watershed method [37] is applied to extract the ranges of topographic features whose peaks are such maxima. The features extracted by their method are considered as an intermediate structure between ridge crest segments and full ridge structures [12]. Although the watershed method effectively extracts surface features, it is not clear how to derive more accurate ridge metrics from such features. Moreover, the accuracy of extracted ridges from this method depends heavily on the interpolation method and resolution used to generate the underlying DEM. Since point measurements are often distributed irregularly over the study area, using grid-based analysis methods tends to average across some topographic details of the surface.

An alternative approach is to generate a triangulated surface model, also known as a TIN, from a raw point cloud. Unlike building a gridded DEM, the generation of a TIN does not require a resampling of the surface and can maintain all information derived from the elevation measurements.

Inspired by previous studies, we design a new method to extract ridge structures from TINs generated from ATM swaths. Unlike previous methods, which relied on ridge detection from laser profiles or image-based analysis, our approach focuses on the extraction of ridge structures in a 3-D context. In contrast with the approach proposed by Petty et al. [12], our method does not require converting the ATM points to grids, which allows us to better extract the extent of the ridges within the swath. In addition, the input parameters of our method allow for more flexibility in extracting ridge characteristics to better suit different sea ice applications, such as momentum transfer modeling, environmental monitoring, and navigability analysis.

III. Data Description

In this work, we use the LiDAR points collected from the OIB ATM [11] to generate triangulated surface models, and we use OIB optical imagery for validation of the LiDAR surface returns. Coincident ICESat-2 elevation data is compared with the elevation model generated from the ATM data to assess the extracted surface features. Here we study a 234-km-long OIB ATM survey collected during fall freeze-up in September 2019. Fig. 1 shows the study area. In our analysis, OIB ATM and ICESat-2 elevations are computed relative to the Earth Gravitational Model 2008 (EGM2008 [39]) geoid.

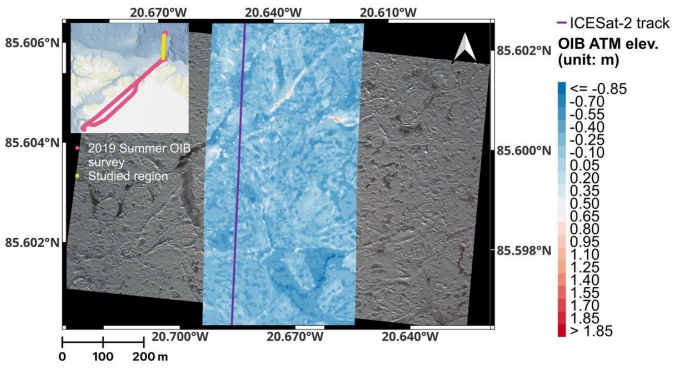

Fig. 1. Example of the datasets used in this study. The basemap is the CAMBOT image from OIB, the mesh layer colored from blue to red is the TIN surface model generated from the OIB ATM dataset, and the purple path overlaying the mesh layer is an ICESat-2 track. The inset map displays the flight path of the OIB survey on September 9, 2019. The basemap of the inset map is the topographic basemap offered by Arctic SDI [38].

A. Operation IceBridge

The ATM is a conical-scanning laser altimeter that collects a swath of point measurements along the path of the aircraft [11]. Two conically-scanning ATM instruments were operated during the survey to collect both wide-scan [40] and narrow-scan [41] data. The wide-scan swath is around 400-m wide with ~0.1 pt/m^2 density [40] and the narrow-scan swath is around 45-m wide with ~0.5 pt/m^2 [41] when flown at the nominal flight altitude of ~500 m. We use the wide-scan data due to its larger swath width and across-track coverage, though the same methodology could also be applied to the narrow-scan data. The wide-scan ATM LiDAR operated at a wavelength of 532 nm, with a laser pulse rate of 5 kHz, and an off-nadir scan angle of 22.5° [40].

The elevation data across the study region, referenced to the EGM 2008 geoid, range ~10 m, and the distribution is positively skewed (Fig. S2a), indicating small areas of heavy deformation. For this study, we have selected a representative 72-km-long region to construct the TIN and extract ridged ice features (~1/3 of the total dataset, Fig. S2b). The average point density, calculated within a 10-m search radius at each point, within the study region is 0.29 pt/m^2, nearly three times the mission requirement of 0.1 pt/m^2 for the OIB ATM wide-scan [40].

Fig. 2(a) shows the distribution of point density at all points within the study region. We visualize the density by assigning density values to the vertices of the TIN (built as described in Section IV-B) and coloring the triangles based on a linear interpolation of the density values at each vertex. A section of the generated map is shown in Fig. 2(b). The point density follows a specific pattern associated with the

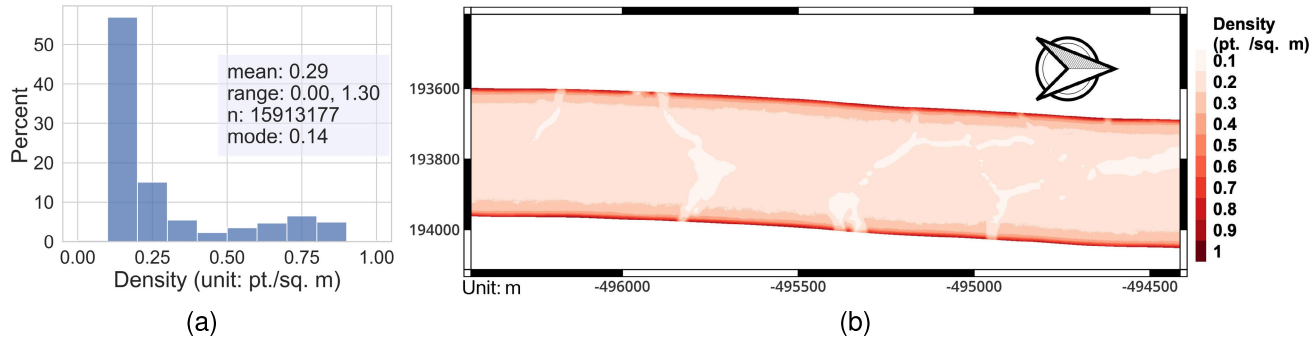

Fig. 2. Point density distribution of the OIB ATM dataset within the study area. (a) Point density distribution within the complete study area (bin width = 0.1 pt/m^2). (b) Density map of a 5-km segment. Due to the ATM scanning mechanism, point densities increase toward the edges of the swath, reaching 0.75–0.85 pt/m^2, indicated by the secondary mode of the distributions in (a). Point densities in the middle of the swath are lower, typically ranging from 0.1 to 0.2 pt/m^2, corresponding to the primary mode of the distributions in (a).

scanning geometry of the ATM laser beam. Density increases toward swath edges (~0.75–0.85 pt/m^2), corresponding to the secondary peak in Fig. 2(a). Density in the middle of the swath is lower, ranging from 0.1 to 0.2 pt/m^2.

There are a few regions with evidently lower point density compared to the surroundings. Previous studies show that specular reflections from very smooth water surfaces and thin ice reflect energy away from the detector, resulting in dropouts in the OIB wide-scan ATM point dataset [42], [43], which causes these regions to have low density. An example of dropouts in a point cloud is shown in Fig. S1, Supplementary Material. These data dropouts lead to regions without enough measurements, such that including these in the surface model can lead to imprecise extraction of topographic features. In Section IV-B, we discuss how to address this issue during the generation of triangulated surface models to best represent the sea ice surface.

High-resolution images, coincident with the ATM data, are collected by the continuous airborne mapping by optical translator (CAMBOT) system during the OIB campaign [19]. The camera is designed to provide images marginally wider than the ATM wide-scan swath. Each CAMBOT image covers an area on the surface ~1000 × ~650 m, has a spatial (pixel) resolution of ~0.2 m, and is both orthorectified and geolocated [19].

B. ICESat-2

One objective of the OIB 2019 summer flight campaign was to obtain observations that had spatiotemporal coincidence with an ICESat-2 overpass [44]. To evaluate ridge results extracted from the TIN, we have selected a 72-km segment of the OIB survey line (highlighted in yellow in Fig. 1) that had the best temporal and spatial coincidence with ICESat-2 reference ground track (RGT) 1123 after a sea ice drift correction was applied. The time difference between the two datasets ranged from 47 to 57 min. We use the University of Maryland-Ridge Detection Algorithm (UMD-RDA) [34] to extract sea ice elevation from the ICESat-2 ATL03 product [45], and we use this to validate the TIN surface model and extracted ridge features from our method. The ICESat-2 elevation profile has a sampling interval of ~0.7 m, a vertical precision of ~0.01 m over flat surfaces [25], and can resolve features as narrow as 5.6 m [34]. Unlike the conical-scanning ATM, which operates at an off-nadir scan angle of 22.5°, ICESat-2 collects data at near-nadir incidence, and thus, avoids the data dropout issue present in OIB wide-scan data.

IV. Methodology

In this section, we introduce the complete workflow for extracting 3-D pressure ridge features from LiDAR point clouds using a surface topology-based method. Section IV-A provides a high-level overview of the proposed processing pipeline. Sections IV-B–IV-E detail the specific computational steps.

A. Method Overview

As illustrated in Fig. 3, the process of extracting ridges from the ATM point cloud consists of six steps as follows.

1) *Step 1:* Generation of TIN of the ice surface through Delaunay triangulation and encoding in the Terrain Trees Library (TTL), as discussed in Section IV-B.
2) *Step 2:* Computation of the surface network, as discussed in Section IV-D.
3) *Step 3:* Topological simplification of the surface network for noise removal, as discussed in Section IV-D.
4) *Step 4:* Extraction of ridge structures from the simplified surface network, as discussed in Section IV-E.
5) *Step 5:* Postprocessing of extracted ridge lines based on a roughness-based filter, which is introduced in Section IV-C.
6) *Step 6:* Output results.

Here, we define the *local level sea ice elevation* as the modal elevation within ~24-km segments. Following previous studies [10], [34], we also define the height above the local level ice surface as the surface elevation anomaly and denote it as H_A. The local level sea ice elevation is subtracted from all ATM measurements to obtain H_A.

B. Triangulated Surface Model Generation

In this section, we describe the generation of triangulated surface models, i.e., TINs, from the ATM point clouds. All ATM elevation points are referenced to the EGM 2008 geoid

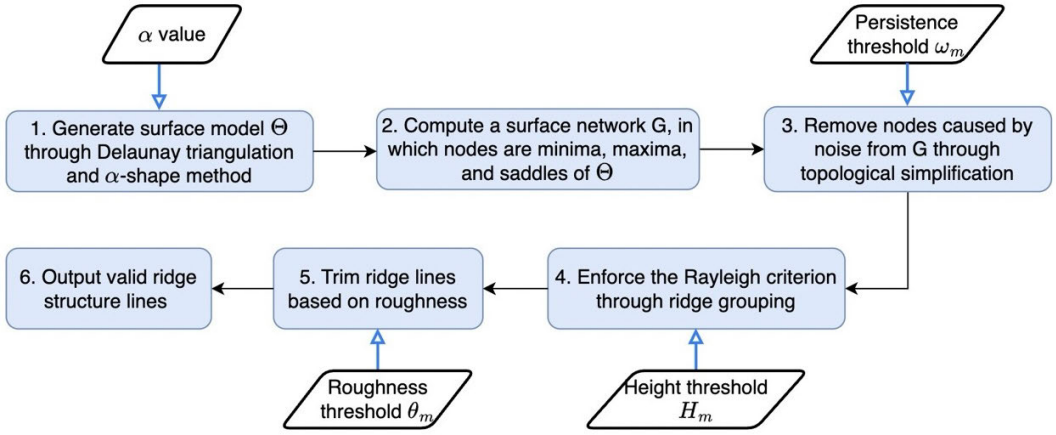

Fig. 3. Flowchart illustrating the steps to generate the ATM-TIN model and to extract ridge structures from the preprocessed OIB ATM points.

and projected to the NSIDC Sea Ice Polar Stereographic North coordinate system (EPSG: 3411).

Delaunay triangulation [17] is the most widely used method for generating a TIN. The Delaunay triangulation of a point set P defines a triangle mesh Σ on the plane, of which the vertices are the points in P and the domain is the convex hull of P [17]. A TIN consists of a mesh Σ generated with Delaunay triangulation, elevations defined on the vertices of Σ, and an interpolating piecewise linear function [46].

The domain of a triangle mesh generated through Delaunay triangulation is always a convex polygon. This leads to elongated triangles at the boundary of TIN, especially when the data coverage domain is not a convex polygon. Such elongated triangles, resulting from artifacts of the triangulation process, do not represent actual sea ice surfaces and thus must be removed. Also, as mentioned in Section III-A, data dropouts over specular surfaces cause measurement gaps. If left uncorrected, these regions would be considered as actual sea ice surface when constructing the topological graph from the TIN-based model. This would lead to false connections across open water and make the extracted features incorrectly extend into data gaps or beyond the valid study area boundaries.

To address these two issues, the α-shape method [18] is applied to the meshes of the generated TINs. The α-shape of a set of points P on the plane depends on the value of the parameter α. Intuitively, the α-shape is obtained from the Delaunay triangulation Σ of P by using a circular eraser with radius α to remove triangles from Σ while ensuring that no points in P are affected. Smaller α values result in the removal of more triangles from the TIN, as smaller α-shapes follow the dataset boundary more tightly. Specifically, when $\alpha = \infty$, the α-shape is the convex hull of P, and when $\alpha \to 0+$, the α-shape is the set of points P [18].

Through experimental evaluations, we determined that an α-value of 20 m effectively removes elongated boundary triangles and dropout-induced artifacts within this dataset, while preserving triangles corresponding to valid sea ice surface measurements. The details of the experiment are explained in Section S2 of the Supplementary Materials. It is worth noting that the selection of α-value varies depending on the dataset and is affected by point density. For this study, a fixed α-value was found to be sufficient for removing the artifacts from the dataset. However, for future work on more general cases, methods for dynamically adapting the α-value based on local point density [47] could offer a more scalable solution.

A new TIN Θ, which is the final surface model, is defined on mesh after α-shape processing with $\alpha = 20$ m with the same elevations at the vertices. Fig. 4 illustrates the effectiveness of this approach in removing most artifacts from the generated TIN. In the following, we refer to the method used to generate a triangulated surface model as the OIB ATM-TIN method, and the generated surface model as the OIB ATM-TIN model. We use the Computational Geometry Algorithms Library (CGAL) [48] for both Delaunay triangulation and α-shape calculations.

The primary challenge in using TINs to represent surfaces is their large storage requirements and high processing costs. Various data structures have been proposed in the literature to encode TINs [49], [50], [51]. In this study, we employ a very efficient data structure for encoding a TIN, named terrain trees [51]. The fundamental concept behind terrain trees is to divide the domain of the TIN into a set of rectangular blocks using a nested subdivision strategy, which can be a kD-tree or a quadtree. Each block b within T encodes the vertices in b and the triangles intersecting b. Terrain trees require approximately 36% less storage than the most widely used data structure for triangle meshes, the indexed data structure with adjacencies [49], with comparable or better time performances [51].

Previous applications of terrain trees [52] also demonstrated their advantages in parallel computing, as different blocks can be processed independently. It is worth noting that, while terrain trees are designed for TINs, their spatial subdivision also facilitates operations on points, such as point query and range query, thanks to the inclusion of a spatial index for efficient coordinate searching. Based on terrain trees, an open-source library providing a range of versatile spatial analysis tools, the TTL has been developed [53].

The existing functionalities of TTL were not originally tailored for sea ice studies. In this work, we extend the capabilities of TTL by modifying existing functions for topological surface analysis and implementing new algorithms based on the operators supported within TTL.

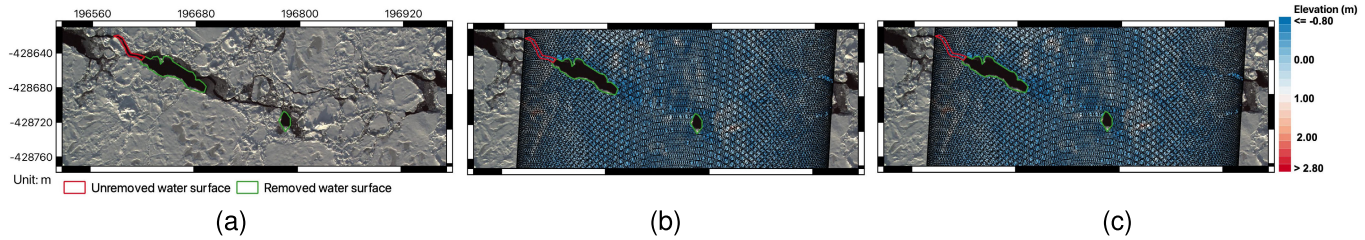

Fig. 4. Correspondence between the open water surface and large triangles in TIN. (a) OIB CAMBOT image showing sea ice region with open water. (b) Corresponding TIN generated from the OIB ATM data. (c) Modified TIN after the underlying mesh is processed with the α-shape method (α = 20 m). The black lines in (b) and (c) depict triangle edges in the mesh. The region highlighted with the green boundary is a water surface region that has been successfully removed from the mesh through the α-shape method. The region highlighted with the red boundary is a water surface region that has not been removed by this method since the triangles forming it have average sizes that are consistent with other triangles in the mesh.

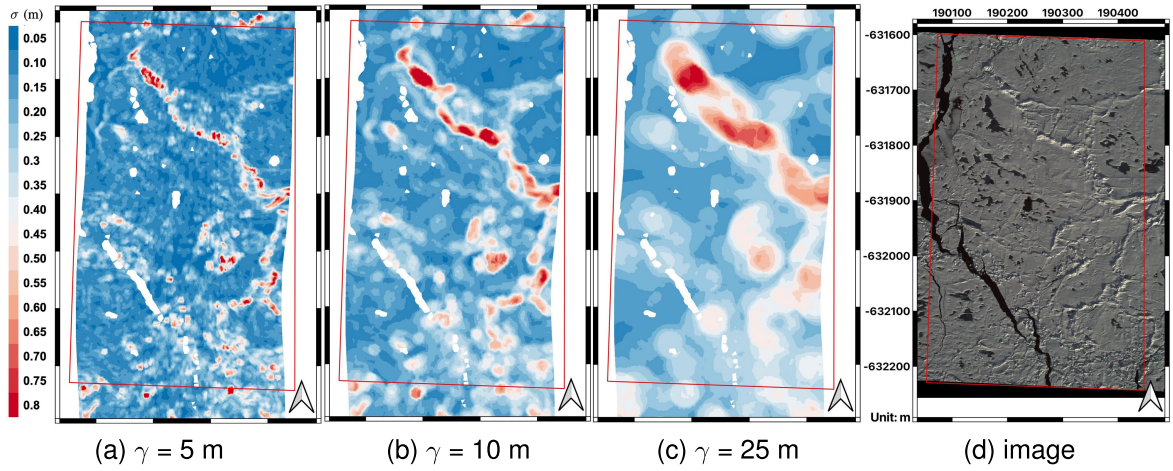

Fig. 5. Roughness and terrain features in an example region. (a)–(c) Roughness maps based on roughness calculated at OIB ATM points using different measurement radii. The roughness at each point is calculated as the standard deviation of point elevations within the circle with radius γ centered at it. (d) Corresponding CAMBOT image for this region. The red boundaries highlight the overlap between the OIB ATM swath and the OIB CAMBOT image.

C. Surface Roughness Calculation

Roughness is a crucial feature of sea ice topography, which has been extensively studied in previous research [25], [34], [35]. Generally, a higher roughness of the sea ice indicates more complex topographic features and, thus, lower navigability. Sea ice roughness is influenced by ice deformation when ice floes collide and, therefore, it is used to identify topographic features such as ridges and leads [54] and to determine areas of level sea ice [10]. In this work, we use a roughness-based filter to distinguish deformed ice from level ice. This filter is applied to the potential ridge structures extracted with the topological method.

There are different definitions of roughness depending on the scale studied and on the data format. In most sea ice studies, roughness is defined as the standard deviation of elevations, but the scales and ranges of elevations vary. For instance, in [25], roughness is defined as the standard deviation of sea ice heights within 25-km-long segments. In [35], roughness is computed as the standard deviation of elevations for each scan line measured by the laser scanner, or the standard deviation of a five-data-point moving window for the single-beam altimeter. In [55], roughness is calculated as the standard deviation of elevation measurements within a 1.1-km resolution pixel.

We define the roughness at a point p as the standard deviation of elevations of all points within a circle C_p centered at p. The selection of radius γ of C_p is critical as it determines the scale of the roughness estimation. If the radius is too small, the roughness can be noisy when there are too few neighbor points or cannot be computed at all if there is no neighbor within C_p. Conversely, if the radius is too large, small isolated elevation changes on the surface are averaged out.

To understand how different scales affect the interpretation of roughness results, we compute roughness with different circle radii γ based on the spatial resolution (footprint sizes) of common airborne and satellite laser altimeters [56]. Fig. 5 shows an example of roughness calculated with different radii (γ = 5, 10, and 25 m) and the corresponding imagery, while the complete result can be found in Section S1-B of the Supplementary Material. In the roughness maps with radii γ = 5 m [Fig. 5(a)] and γ = 10 m [Fig. 5(b)], a correlation emerges between high roughness values (indicated by the red areas) and topographic features, such as ice hummocks and ridges that are visible in the image [Fig. 5(d)]. While in the roughness map with γ = 25 m [Fig. 5(c)], many small features are averaged out. Based on this analysis, we select a radius γ = 5 m to calculate the roughness as it can effectively capture elevation variations of small sea ice features.

The computed roughness field is then used as a filter for trimming the extremities of extracted feature lines. Specifically, the terminal segments of topological lines are excluded from ridge structures if their roughness is lower than a certain

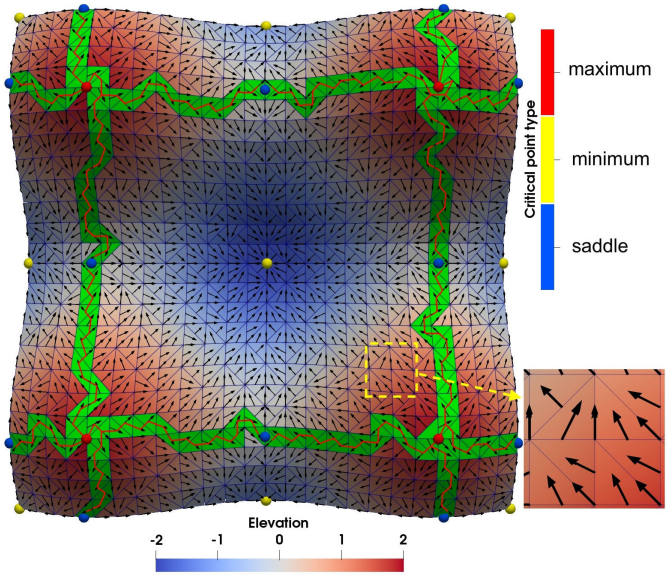

Fig. 6. Example of a discrete gradient vector field calculated from a triangulated surface with an elevation function. The gradient vector field is calculated following the definition in discrete Morse theory [58], [59]. Spheres on the figure correspond to the centroids of critical vertices, edges, and triangles in the discrete gradient field. Red spheres are maxima (critical triangles), blue spheres are saddles (critical edges), and yellow spheres are minima (critical vertices). The green triangles are the triangles along the gradient paths between maxima and saddles following the pairs in the gradient vector field. The red lines connecting the centroids of such triangles correspond to the geometry of maxima-saddle arcs in the surface network G (introduced in Section IV-D1 in more detail).

value, as elevation variation is expected to be significant along ridges.

D. Surface Network and Topological Simplification

1) Surface Topology and Ridge Structure: The foundation of our method is a labeled graph representation of the surface topology, called a surface network (G). This network is derived using principles from discrete Morse theory [16], which identifies critical points, minima, saddles, and maxima, and gradient paths joining them on the TIN surface. As illustrated in Fig. 6, maxima correspond to local elevation peaks, saddles to pass points between peaks, and minima to local depressions.

In the surface network G, nodes represent critical points, and the arcs represent gradient paths connecting saddles to minima or maxima, indicating lines of steepest descent. The geometry of these paths is represented as a chain of line segments connecting the centroids of adjacent triangles (for maximum-saddle arcs) or vertices (for saddle-minimum arcs) in the mesh.

Similar to previous studies on ridges, we consider a local maxima on the surface whose elevation anomaly H_A is higher than a height threshold H_m as a ridge peak. A maximum may have multiple arcs originating from it, and one saddle must be connected to exactly two maxima by definition. We define a potential ridge structure as the subset of geometries of the arcs from such a maximum to connected saddles. But the existence of noise and small surface features gives rise to spurious topological features. As shown in Fig. 7(a), a surface network calculated from the TIN includes overly abundant nodes even in a small region (206 maxima and 423 saddles in an 140 $\times$ 140-m region). Thus, a preprocessing step to remove noise and critical points caused by natural elevation fluctuations is required.

2) Topological Simplification: Nodes representing noise or insignificant surface features in a surface network can be removed through topological simplification. Discrete Morse theory introduces an operator called topological cancellation for this purpose [16]. For a surface network G, there are two cancellation operators, maximum-saddle-maximum and minimum-saddle-minimum.

Given two maxima M_a, M_b, and a saddle S adjacent to both maxima in a surface network G, maximum-saddle-maximum cancellation removes M_a, S, and the arc connecting them. Other saddles adjacent to M_a, if they exist, are connected to M_b after the removal of arc $M_a \rightarrow S$. If such saddles exist, then we call M_a an *internal* maximum. Otherwise, we call M_a a *boundary* maximum. For instance, M_4 in Fig. 8(a) is a boundary maximum, and thus, no other saddle is reconnected to M_1 after M_4 and S_2 were removed [as shown in Fig. 8(b)]. Arcs connected to the removed saddle and maximum in G are removed at the same time. Conversely, when an internal maximum like M_1 in Fig. 8(a) and its adjacent saddle S_1, are removed, arcs connected to S_1 are removed, and all other saddles adjacent to M_1 (i.e., S_3) are reconnected to the other maxima M_2 [as shown in Fig. 8(c)]. After cancellation, the geometry of arc $M_2 \rightarrow S_3$ becomes a chain merged from the geometries of three arcs in the original graph ($M_2 \rightarrow S_1$, $M_1 \rightarrow S_1$, and $M_1 \rightarrow S_3$). The change in the surface network caused by a maximum-saddle-maximum cancellation corresponds to the changes in the underlying gradient vector field. All arrows along the gradient path corresponding to the removed arc $M_a \rightarrow S$ are reversed, and thus, the gradient path no longer exists.

The minimum-saddle-minimum cancellation, boundary minimum, and internal minimum are similarly defined. Both cancellation operators operate only on the surface network G, and thus the underlying mesh is not modified.

The removal of boundary and internal critical minima and maxima has different effects on the ridge extraction result. Assuming that the maximum M_2 is a valid ridge peak, the arcs starting from M_2, which are the initial structure of the ridge peaking at M_2, are highlighted in red in panels of Fig. 8. In both Fig. 8(b) and (c), a saddle connected to M_2 is removed, together with the other maximum connected to this saddle. When the removed maximum is a boundary maximum [M_4 in Fig. 8(a)], the structure is reduced after cancellation since arc $M_2 \rightarrow S_2$ was removed. In contrast, when the removed maximum is an internal maximum [M_1 in Fig. 8(a)], the structure grows larger since the geometry of arc $M_2 \rightarrow S_3$ consists of the geometries of three arcs.

A common criterion to decide if an arc should be removed or not is the elevation difference between the two nodes connected by the arc [57]. The magnitude of the absolute elevation difference between a pair of adjacent nodes in G is also called the persistence of this pair of nodes, denoted as ω. When the persistence of a pair of adjacent nodes is

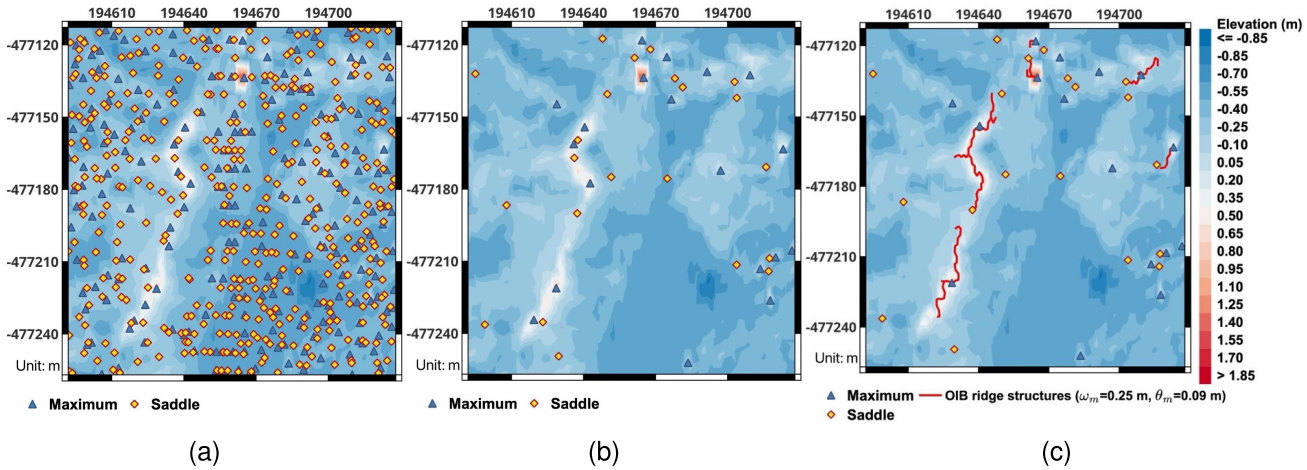

Fig. 7. Illustration of how the distribution of maxima and saddles in the discrete gradient vector field changes during the ridge extraction process. (a) Maxima and saddles in the original field were calculated from the TIN. (b) Maxima and saddles after the topological simplification (ω_m = 0.25 m). (c) Maxima and saddles after the ridge grouping and roughness filtering (θ_m = 0.09 m) steps. The red lines in (c) are final ridge structures extracted with the proposed method. These figures show that the original gradient vector field contains overly abundant maxima and saddles due to background noise and small topological features on the sea ice surface. Our ridge extraction method effectively removes most of these insignificant features.

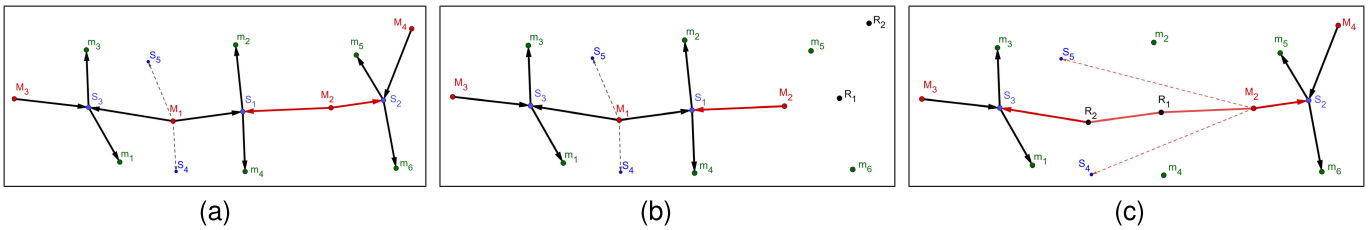

Fig. 8. Example of a maximum-saddle-maximum cancellation operation on a surface network G. Red points with M- prefix are maxima, blue points with S- prefix are saddles, green points with m- prefix are minima, and black points with R- prefix are regular vertices, edges, and triangles. The lines are the arcs connecting those nodes in G, which indicate the gradient paths in the discrete gradient vector field. The arrows indicate direction along the path. The red lines highlight arcs starting from maximum M_2. Note that the regular points are not a part of the surface network and are just displayed for illustration purposes. (a) Original surface network, G. (b) Surface network when the cancellation operator is performed on a boundary maximum M_4 and a saddle S_2 adjacent to it. Both M_4 and S_2 become regular points after the cancellation, and arcs connected to them are removed from G. (c) Surface network when the cancellation operator is performed on an internal maximum M_1 and a saddle S_1 adjacent to it. Both M_1 and S_1 become regular points after the cancellation. The arc between them is reversed, and the three arcs of the same direction ($M_2 \rightarrow S_1$, $M_1 \rightarrow S_1$, and $M_1 \rightarrow S_3$) are merged into one ($M_2 \rightarrow S_3$). Other saddles connected to M_1 are reconnected to M_2, and other arcs connected to S_1 are removed from G.

small enough, we remove the two nodes from G since they are not significant surface features. Fig. 7(b) shows the result of topological simplification when ω_m = 0.25 m. We observe that most maxima and saddles in flat regions are removed, while maxima with evident elevation difference from the neighborhood and saddles separating those maxima are kept. In Section V, we discuss how the selection of the persistence threshold ω_m affects the ridge extraction result.

E. Ridge Structure Extraction

After topological simplification, the potential structure of a ridge can be extracted as a collection of geometries of arcs connected to a maximum M. Such collections are processed in a final, multistage procedure to identify valid ridge peaks and refine the ridge structures.

First, a maximum is selected as a potential ridge peak only if its surface elevation anomaly (H_A) exceeds a height threshold H_m. The selection of H_m is discussed in Section V.

Next, since a ridge can contain several maxima (peaks), we apply the *Rayleigh criterion* [36] through a process we term *ridge grouping* to identify peaks that belong to the same ridge. This step evaluates two adjacent maxima in the surface network G that are connected to the same saddle. If two maxima are not at least twice as high as the saddle connecting them, the structure associated with the lower maximum is merged into that of the higher maximum. Similar to the topological simplification, the merging can be handled through a cancellation operator. Specifically, given a saddle S, and two maxima M_1 and M_2 adjacent to S in G, M_1 and S can be removed through cancellation if and only if it follows.

1) The elevation anomaly H_A of M_2 is higher than that of M_1.
2) H_A of M_2 is higher than a surface elevation anomaly threshold H_m (H_m = 0.6 m, see Section IV-E).
3) H_A difference between M_2 and S is less than half of the H_A of M_2.
4) M_1 is not a boundary maximum.

All triplets $\{M_1, S, M_2\}$ are sorted in descending order with respect to the elevation anomaly H_A of the highest

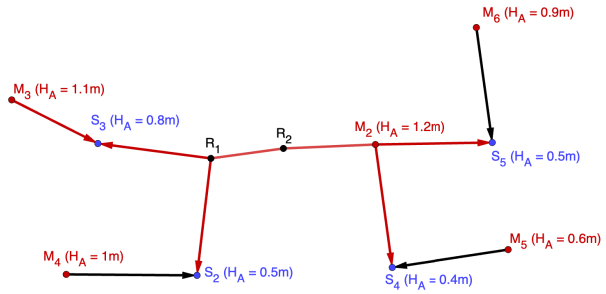

Fig. 9. Example of ridge grouping. Red points with M- prefix are maxima, blue points with S- prefix are saddles, and black points with R- prefix are regular vertices, edges, and triangles. The lines are the arcs connecting those nodes in G, which indicate the gradient paths in the discrete gradient vector field. The arrows indicate direction in the vector field along the gradient paths. The red lines are the ridge structure of maximum M_2 extracted by our method. Note that other regular points along the gradient paths are not shown in this figure. The elevation anomaly H_A of a node is the anomaly of the highest vertex of the corresponding geometry. With the given anomalies in the graph, the ridge structures of M_3 should be merged to that of M_2 according to the discussion in Section IV-E.

maximum in the triplet. In other words, maxima adjacent to the highest maximum in the study region are investigated first to ascertain if they should be removed. Condition (4) is necessary to avoid the unintended removal of ridge structures at dataset boundaries. For instance, in the case shown in Fig. 9, when M_3 and S_3 are removed, the ridge structure of M_3 ($M_3 \rightarrow S_3$) is discarded instead of being merged to the structure of M_2. We avoid removing a boundary maximum to maintain the completeness of the ridge structure. Instead, we add the ridge structure of a boundary maximum like M_3 to the structure of its adjacent maximum M_2 when M_3 only satisfies conditions (1–3).

Finally, the resulting ridge structure lines, which often extend beyond actual ridge boundaries into adjacent level ice regions, are trimmed using a 5-m roughness filter as introduced in Section IV-C. Specifically, we check the geometry of each arc starting from the maximum, and terminate the chain once all vertices of a triangle have a surface roughness (at $\gamma = 5$ m) that is less than a predefined threshold θ_m. In Section V, we discuss how the selection of θ_m affects the ridge extraction results and how we decide to set $\theta = 0.09$ m.

Fig. 7(c) shows the result obtained when the ridge grouping step and the roughness filter have been applied to the result in Fig. 7(b) when $\theta_m = 0.09$ m. The figure illustrates that a few peaks along the higher elevation regions are removed, and thus, the final ridge structure consists of longer paths and better describes the overall ridge.

V. Parameter Calibration

In this section, we discuss how the input parameters affect the ridge extraction results, and we define how these parameters are selected. There are four parameters in the ridge structure extraction algorithm: the alpha value α for the surface model generation process, the persistence threshold ω_m for the topological simplification, the peak height threshold H_m for selecting valid ridge peaks, and the 5-m roughness threshold θ_m for the roughness filter (Fig. 3). The selection of α has already been discussed in Section IV-B. The peak height threshold H_m is set to 0.6 m following previous studies [10], [25], [33] to exclude smaller sea ice features. More generally, for regions with significantly different ice characteristics, H_m can be selected by minimizing the deviation between the observed ridge height distribution and theoretical models (e.g., a negative exponential function [33]).

In the following of this section, we focus on the selection of ω_m and θ_m. Two independent ridge datasets obtained from other methods are used to compute the metrics for features computed from our method and to select ideal parameters. The first, denoted R_I, is comprised of ridge crests extracted from spatiotemporally coincident ICESat-2 surface elevation measurements as determined by the UMD-RDA [10]. The second, denoted R_M, consists of ridge sails visually extracted from six CAMBOT images in the study area. Inspired by previous studies [10], [30], the visual inspection of ridges is performed by identifying lines separating the level ice surface from shadows cast by ridge sails in the optical images. Lines that pass through any area higher than 0.6 m are added as valid ridge lines to R_M. Note that while R_I is a set of points representing ridge crests, R_M is a set of lines representing the ridges themselves. Ridge structures extracted from the OIB ATM-TIN model using our method are denoted R_A.

The modal roughness for level ice ($H_A \leq 0$) calculated at $\gamma = 5$ m is 0.09 m in the 72 km-long study segment. This value represents the background noise in roughness, comprising sensor noise and minor surface features like sastrugi. Thus, we select it as the maximum roughness threshold to test in our experiments to avoid removing significant features.

Recall that the persistence ω is used in the topological simplification step and is the elevation difference between two nodes connected by an arc in the surface network G. Since the goal of topological simplification is to remove noise and small variations on the surface, the maximum value of ω_m to be tested in the experiments should be less than H_m, otherwise the topological simplification would remove valid ridges from the extracted paths. Thus, the maximum ω_m to test in the experiments is set to 0.5 m. We extract ridge structures using different combinations of θ_m and ω_m values. The parameter θ_m is varied in increments of 0.01 m, ranging from 0 to 0.09 m, while ω_m is varied in increments of 0.05 m, ranging from 0 to 0.5 m.

Two criteria are considered when selecting the parameters for ridge extraction in this study: 1) the number of the extracted ridges in R_A; and 2) the ratio of R_A to the equivalent (matching) ridges in independent datasets R_M and R_I.

A. Influence of Parameters on Extracted Ridge Number

We evaluate the impacts of ω_m and θ_m on the number of extracted ridges in R_A that are within the data collection ranges of independent datasets R_I and R_M. Results are shown in Fig. 10(a) and (b). We consider the range of R_I as a 5-m buffer zone around the ICESat-2 track in the study region. The range of R_M is six inspected images, i.e., six ~400 × ~650-m rectangles.

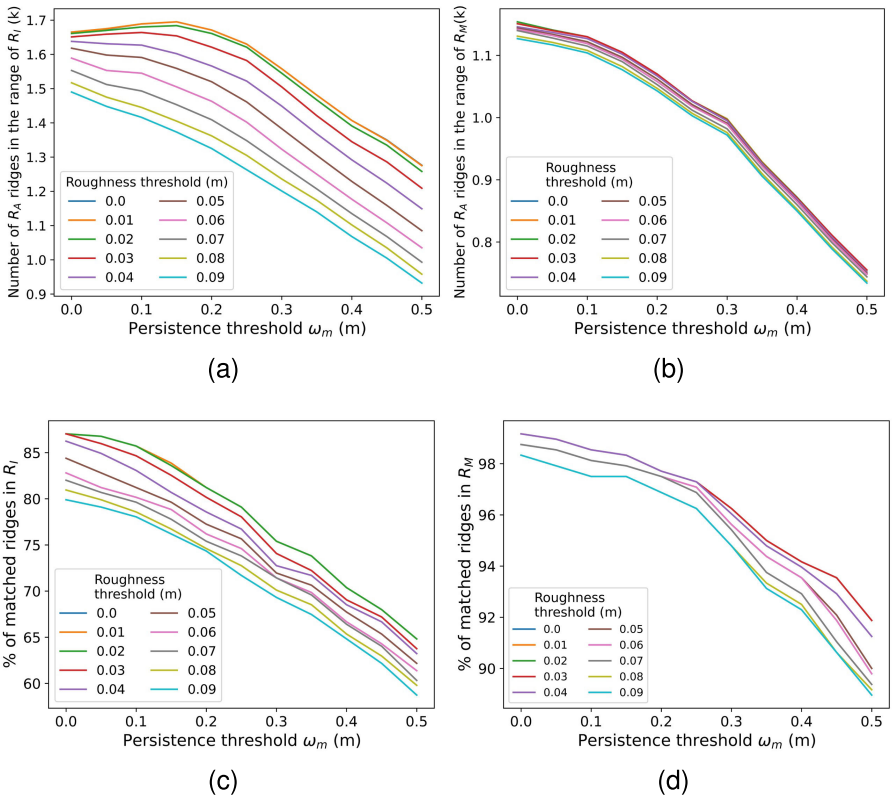

Fig. 10. Trends in the statistics of ridge lines extracted with our method as the roughness threshold θ_m and persistence threshold ω_m change. Relationship between θ_m and ω_m and (a) total number of R_A ridges that intersect with the 5 m buffer zone around the ICESat-2 track, (b) total number of R_A ridges within the range of six visually inspected images, (c) percentage of R_I ridges that have a match in R_A, and (d) percentage of R_M ridges that have a match in R_A. R_I: ridge peaks extracted from the ICESat-2 profile with the UMD-RDA [10]. R_M: ridge lines visually extracted from six CAMBOT images in the study area. R_A: ridge structures extracted from the OIB ATM-TIN using our method.

In general, an increase in ω_m results in fewer R_A ridges within the ranges of both datasets R_I and R_M. The only exception occurs when both ω_m and θ_m are small ($\omega_m \leq 0.15$ m and $\theta_m \leq 0.02$ m). Under these conditions, increasing ω_m leads to more R_A ridges within the range of R_I. This unexpected outcome can be explained by the effect of topological simplification and the way we count ridges. As discussed in Section IV-D, though topological simplification consistently removes maxima and saddles, it can also lead to longer ridge structure lines. Thus, it is possible that the number of R_A ridges intersecting a region goes up when the total number of R_A ridges goes down. Indeed, the relationship between the total number of R_A and ω_m (not displayed here) shows a consistent negative correlation.

The value of θ_m and the number of ridges in the validation dataset range also show a negative correlation. An interesting observation is that the difference in the number of R_M is considerably less significant compared to that of R_I. A plausible reasoning is that the roughness filter typically only trims the ridges rather than removing them completely, unless the entire length of a ridge falls within low 5-m-roughness regions. Considering that the range of R_I spans a 10-m $\times$ 72-km band, whereas the range of R_M is ~400 $\times$ ~650-m rectangles, the number of R_A ridges intersecting the range of R_I is more likely to be influenced by the reduced ridge lengths due to its narrower range.

B. Influence of Parameters on the Number of Matching Ridges in R_A and the Validation Datasets

We explore the relationship between ω_m and θ_m and the percentage of ridges identified in both independent datasets. A ridge peak R_i from R_I is considered to match with a ridge structure R_a in R_A if R_a intersects with a 5-m buffer zone around R_i. Similarly, a ridge R_m from R_M is considered to match with a ridge structure, $R_{a'}$ in R_A if $R_{a'}$ intersects with a 2-m buffer zone around R_m. We find that increasing the persistence threshold ω_m leads to a lower percentage of matching ridges between R_A and both validation datasets [see Fig. 10(c) and (d)]. This can be explained by the decrease in the number of ridges when a larger ω_m is used. We also notice that when ω_m is smaller than 0.15 m, the decline in the number of ridges in R_A that match with R_M is less pronounced. This phenomenon suggests that a large ω_m is more likely to significantly impact the results and agreement between the datasets. When comparing different roughness thresholds θ_m, we observe that higher θ_m values tend to result in lower percentages of matching ridges in the independent datasets. Similar to the reasoning for ω_m, some ridges are shortened or removed by the roughness filter, resulting in poorer alignment with the independent datasets. Thus, the percentages of matching ridges appearing in both R_I and R_M decrease as θ_m increases. In addition, we find that the impact is much less significant when θ_m is small (e.g., $\leq$ 0.02 m),

likely because there are few areas in the study region with such a low 5-m roughness.

C. Discussion on Parameter Selection

Methodologically, roughness threshold θ_m determines the sensitivity of the postprocessing filter and how many feature lines should be removed from the ridge results. Our experiment confirms the negative correlation between θ_m and the ridge length/number. Lower thresholds caused ridge lines to extend artificially into the surrounding level ice, while higher thresholds caused an underestimation of the ridges' true spatial extent. In this work, we cap the roughness threshold at 0.09 m, which is the modal roughness for level ice, to avoid the latter case from happening, and compare results extracted with different other threshold values to find the one leading to the best-matching results. To adapt this workflow to other regions or seasons, we recommend determining θ_m dynamically by analyzing the roughness distribution of the local level ice and selecting the modal value as the noise floor.

The effect of persistence threshold ω_m is more complex as it works on the surface topology instead of surface model geometry. In our experiments, lower ω_m values left the surface topology to be noisy, and small features and data noise were included in the final ridge results. Conversely, higher ω_m values caused the surface topology to be over-simplified or over-smoothed, and lower relief ridges were removed or merged with neighboring ridges incorrectly. We selected an intermediate value that optimized the tradeoff between stabilizing the total ridge count and maintaining a high matched ridge ratio against validation data.

The selection of parameters (ω_m and θ_m) depends on the specific requirements of the applications and end users. In this study, the focus is on achieving a higher ridge match ratio without overestimating surface complexity. Therefore, from the results of all combinations of ω_m and θ_m, we select the pair of parameters that ensures 95% of ridges in R_A match with those in R_M and 70% of ridges in R_A match ridges in R_I. Following this rule, $\omega_m = 0.25$ m and $\theta_m = 0.09$ m are used for ridge extraction in the following experiments.

VI. Results

In this section, we evaluate our method by validating the generated surface model and the extracted ridge features against ICESat-2 ATL03 data [45] and OIB CAMBOT optical imagery [19]. Section VI-A accesses the accuracy of the TIN-based surface model by comparing its elevations with a coincident ICESat-2 profile. We also validate the artifact removal process by comparing the spatial extent of the surface model against CAMBOT imagery. Section VI-B presents the ridge extraction results obtained when using the optimal parameters selected in Section V.

A. Surface Model Validation

To validate the accuracy of the generated surface model Θ, we compare the elevation profile of ICESat-2 calculated using the UMD-RDA method [25] with a profile generated from Θ by interpolating Θ at the ICESat-2 UMD-RDA sampling points along the ICESat-2 RGT. This interpolation is performed using the piecewise linear function [46] inherent to the TIN model. Specifically, for any point that falls within a triangle t of Θ, its elevation is calculated through the barycentric interpolation based on the three vertices of t. As mentioned in Section III-B, a sea ice drift correction was applied to the ICESat-2 data before the comparison.

Fig. 11 displays two elevation profiles along a 1 km segment of the RGT. The two surface elevation profiles follow each other closely and reveal a highly complex, rough sea ice surface with large, abrupt elevation deviations corresponding to sea ice pressure ridges. The OIB ATM-TIN and ICESat-2 UMD RDA elevation profiles appear to be strongly correlated with only minor elevation differences in some areas. For instance, in segment (I) in Fig. 11(a), the OIB ATM-TIN profile exhibits a short area of low-elevation, evidently lower than the corresponding ICESat-2 elevation estimate. This discrepancy occurs at a small feature (~5 m in length) on the sea ice surface [Fig. 11(b)] and arises due to the higher resolution OIB ATM data with respect to the ICESat-2 observations. The OIB ATM-TIN method allows small features like old melt ponds and small cracks (even in mélange areas) to be resolved, whereas ICESat-2 struggles to resolve these small features due to its larger footprint. A second example of an elevation difference can be observed in segment (II) in Fig. 11(a). In segment (II), the ICESat-2 profile consistently maintains a low elevation, while in the OIB ATM-TIN profile, there is a sharp elevation change in the middle of the segment. As shown in Fig. 11(c), segment (II) corresponds to a crack in the ice known as a lead where open water is exposed. Here, the difference between the two profiles is caused by the errors in the OIB ATM-TIN due to data dropouts over the open water. In contrast, the ICESat-2 dataset performs well over leads and can even distinguish the elevation differences between thin ice and open water. In Fig. 11(d), we compare elevation distributions from the two methods after the removal of outliers, defined as elevations falling beyond two standard deviations from the mean. The result shows that the elevations derived from the two methods are highly correlated (with a correlation coefficient $r = 0.75$) with mean and modal differences of -0.05 and -0.03 m, respectively, close to the cm-level precision of the input datasets. Small discrepancies are most likely due to sea ice drift in the short time that elapsed between the acquisition of the two datasets.

As mentioned in Section IV-B, removing artifacts in the generated surface model is critical to extract ridge lines correctly. To validate the strategy, we analyzed the geometric difference between the initial domain of TIN and the domain of the final surface model Σ, i.e., the one processed with the α-shape method. By comparing the removed regions against coincident CAMBOT imagery, we confirm that they consistently correspond to surfaces of open water or regions outside the data range. Among these removed regions, we distinguish internal data dropouts from boundary artifacts using a filtering method described in Section S3 of the Supplementary Material. By comparing internal data dropouts against coincident CAMBOT images (e.g., Fig. 12), we confirm that they all correspond to surfaces of open water or very thin ice (termed "nilas"). Open

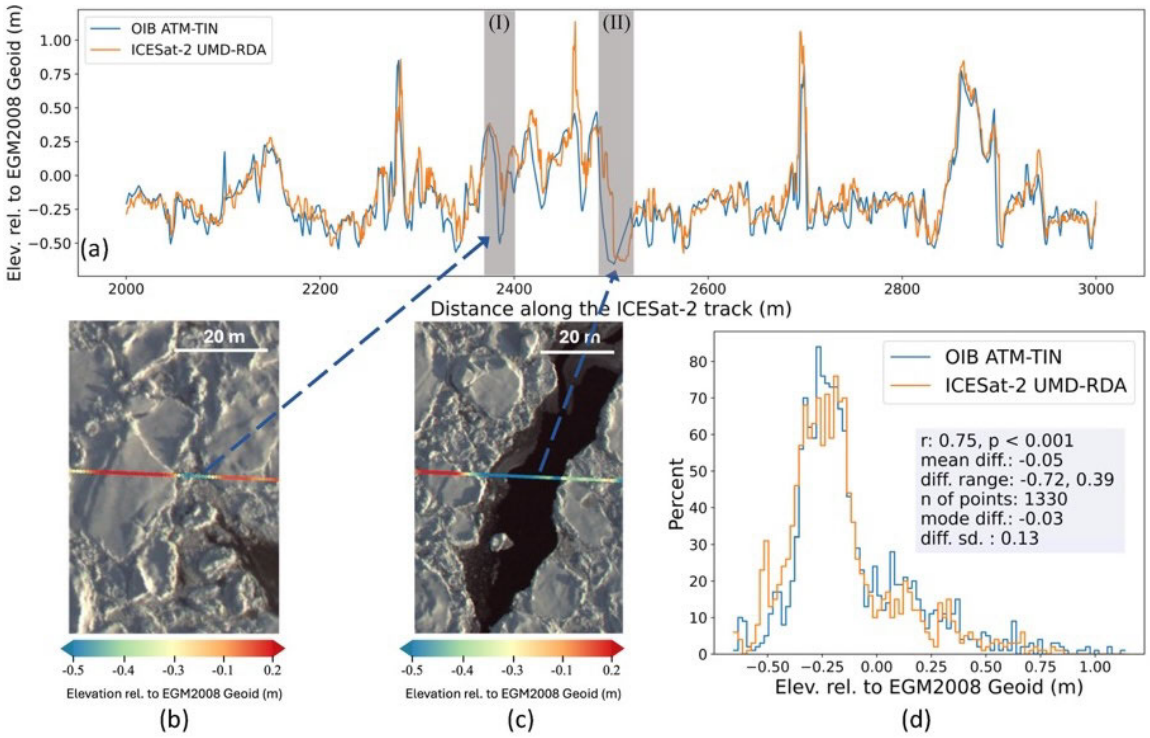

Fig. 11. Comparison between surface elevations derived using the OIB ATM-TIN model and the ICESat-2 UMD-RDA. (a) Elevation profiles from the interpolation of the OIB ATM-TIN model along the ICESat-2 track (blue line) and the UMD-RDA applied to ICESat-2 ATL03 data (orange line) along a 1-km segment. (b) and (c) Two examples of surface features where discrepancies between the OIB ATM-TIN and the ICESat-2 UMD-RDA profiles are observed. In (b), a small surface feature such as brash ice is detected in the OIB ATM-TIN model, but cannot be detected in ICESat-2 UMD-RDA. In (c), an open-water region leads to data dropouts in the OIB ATM data and an error in the OIB ATM-TIN model. (d) Surface elevation distributions derived from the profiles shown in (a). Points whose elevation measurement is out of the range ($mean - 2 \times sd.$, $mean + 2 \times sd.$) in either distribution are excluded as outliers.

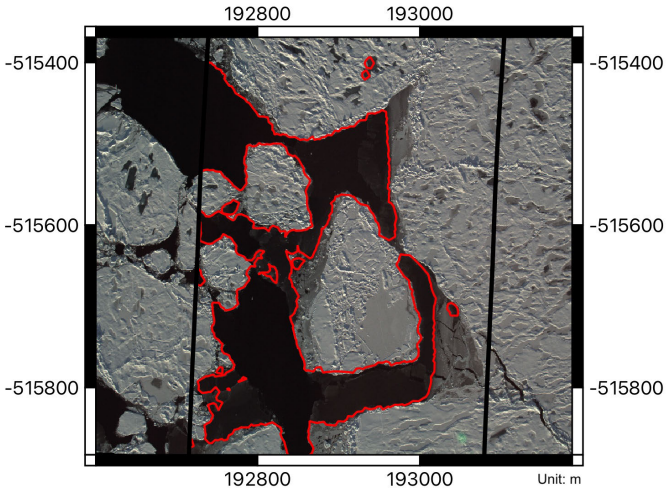

Fig. 12. Example of data dropouts removed during the surface model generation step (see Section IV-B). These regions (outlined as red polygons) are identified as internal to the OIB ATM data range using the method described in Section S3 of the Supplementary Material. The underlying image is an OIB CAMBOT image of an area with both sea ice floes (gray) and open water/thin ice (dark gray and black). The black vector boundary indicates the range of the OIB ATM data. The comparison between the underlying image and red polygons shows that the regions without measurements match open water or thin ice surfaces.

water/thin ice surfaces extracted with this method account for 1.5% of the total study area (1.24 km^2 out of 82.5 km^2), consistent with typical values for open water areas in Arctic sea ice.

All the operations on TINs are implemented in the TTL [53] and geometry operations like computing the intersection between a circle and D and computing the geometric difference are implemented with Shapely [60] and GeoPandas [61] libraries.

B. Ridge Extraction Results

1) Comparison Between Ridges Extracted From the OIB ATM-TIN and Those Identified in ICESat-2: As mentioned in Section IV-B, we can calculate a profile from the OIB ATM-TIN model along the ICESat-2 track through interpolation. Fig. 13(a) shows a 1-km segment of profiles from the OIB ATM-TIN model and the ICESat-2 UMD-RDA. Within this segment, five ridges are detected by the UMD-RDA, i.e., they exist in R_I. By comparing these five ridges to the ridges extracted from the OIB ATM-TIN model (i.e., ridges in R_A), we find that all five ridges in R_I match those in R_A.

Fig. 13(b) presents a map of extracted ridge structure lines within the selected segment. The result shows that the most pronounced ridges, i.e., those that can be visually identified in the OIB ATM-TIN, are identified using our proposed method. Numerous short ridge segments are observed, which are common in areas where sea ice dynamics are prevalent. Convergence between ice floes causes fracturing, and often,

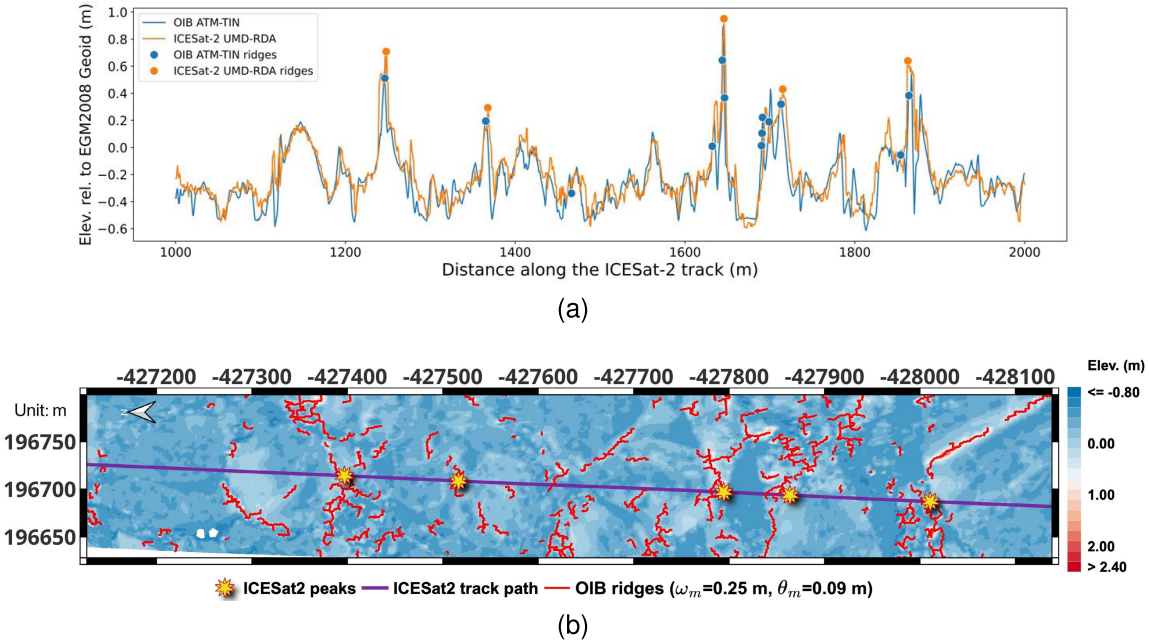

Fig. 13. Comparison of ridges detected with the OIB ATM-TIN model and the ICESat-2 UMD-RDA. (a) Elevation profiles from the interpolation of the OIB ATM-TIN model along the ICESat-2 track (blue line) and the UMD-RDA applied to ICESat-2 ATL03 data (orange line) in a 1-km segment. Orange circles indicate the ridge peaks identified by UMD-RDA, and the blue circles indicate the intersections between the extracted ridges from the ATM-TIN model and the ICESat-2 track. (b) Elevation map of the OIB ATM-TIN model with ridge lines extracted by our method displayed as red lines.

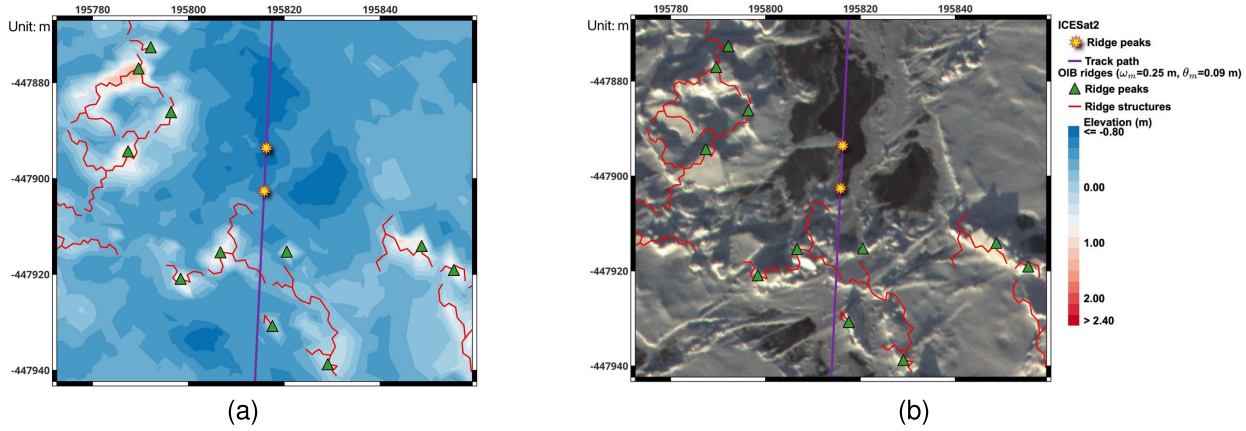

Fig. 14. Case in which the ridge sails detected with the ICESat-2 UMD-RDA [10] diverge from the results of our method applied to the OIB ATM-TIN model. The two stars in the figures are ridge peaks extracted with UMD-RDA, but our method does not detect any ridge line around them. This disagreement is due to the time difference between the acquisition of the ICESat-2 and OIB ATM observations and sea ice drift in the intervening time period, which, if not precisely corrected, can result in a misalignment between the two datasets. (a) Elevation map of OIB ATM-TIN model with ridge lines extracted with our method (red lines). (b) CAMBOT image of the same area as shown in (a).

large ice floes fragment into smaller pieces. These small floes are pushed upward from the pressure, causing a floe edge to protrude above the local level ice surface. A divergence event (i.e., opening of a lead between two floes) can cause these small upturned floes to drift away, where they are eventually refrozen into the new ice growing elsewhere.

Conversely, Fig. 14 shows an example of ridges that are indicated in the ICESat-2 UMD-RDA elevation profile but that are not identified by the ATM-TIN method. In Fig. 14(a), the two ridges detected in the ICESat-2 data are actually associated with melt ponds, which can be seen in the OIB CAMBOT image [Fig. 14(b)]. This result is likely caused by sea ice drift between the acquisition times of the two datasets. Although a drift correction has been applied, it is based on a best estimate of ice motion between the two data acquisitions, and due to floe rotation, it cannot ensure a perfect match at all locations along the track. Unmatched ridges, such as this case, can be identified by selecting ridge peaks with very low elevation anomalies H_A in the OIB ATM-TIN model. For instance, among 107 ridge peaks in R_I that do not match ridges in R_A, 43 of them have H_A <= 0 m in the OIB ATM-TIN model.

2) Comparison Between Ridges Extracted From the OIB ATM-TIN and Those Visually Selected From the OIB CAMBOT Imagery: In Fig. 15(a), we compare ridges in R_A with ridge lines picked out through visual inspection, i.e., ridges in R_M. As we can see from the figure, the major ridge in the middle of the region has been identified by our proposed method, and the

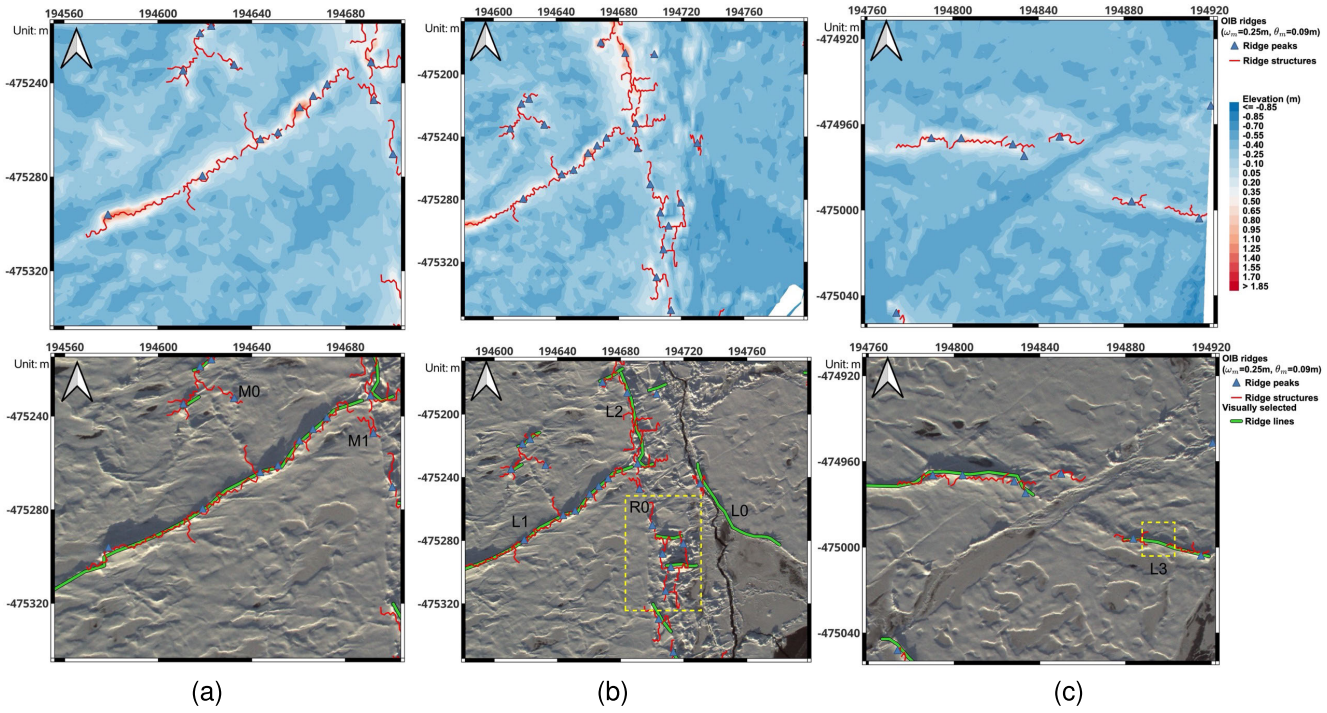

Fig. 15. Example of ridge extraction results with ω_m = 0.25 m, θ_m = 0.09 m. (a) Example where the ridge results from the visual inspection match well with ridges extracted from our method operated on the OIB ATM-TIN model. Ridge peaks M_0 and M_1 are identified by our method, but are hard to detect in images. (b) and (c) Examples where there are discrepancies between the ridge results from the visual inspection and our method. The upper figure for each example is the elevation map of the ATM TIN model, and the lower figure is the OIB CAMBOT image coincide with the OIB ATM data. The yellow dashed box R_0 in (b) highlights a region with complex terrain features, and our method is able to identify such features as ridge lines. L_1 and L_2 in (b) are ridges that are identified by both methods, while L_0 is only identified from visual inspection but not by our method. A possible explanation is that the ridge is too narrow so that no elevation point is collected from its crest. The yellow dashed box in (c) highlights a part of the visually selected ridge line L_3 with low elevation, and thus, is not identified as a part of the ridge line by our method. A more detailed analysis can be found in Section VI-B.

extracted ridge structure lines match well with the ridge line in R_M. Moreover, our method also indicates small ridges that are difficult to identify through visual inspection. For instance, maxima M_0 and M_1 in the image are two ridge peaks detected by our method, but they are hard to identify in the image as their ridge lines are short and the shadows surrounding them are not evident.

In Fig. 15(b) and (c), we show another two factors that can lead to a discrepancy between R_A and R_M. Within Fig. 15(b), we can see that most ridge lines in R_M match well with ridge structures in R_A. For instance, it successfully extracts the ridge lines on the left half of the shown range, like L_1 and L_2, even in complex regions (like the region highlighted with a yellow dashed box). One exception is the ridge line L_0 from R_M. A ridge peak on L_0 has been detected correctly by our proposed method. The extracted ridge structure, however, does not fully align with the visually identified ridge line. When checking the TIN of the study region, we notice that along L_0, there are significant variations in elevation. A few distinct low points along L_0 prevent the extension of the ridge structure lines along this path during the extraction. Besides, the long shadow above L_0 indicates that the elevation of the ridge is evidently higher than the local level sea ice, while it is not evident in the ATM-TIN model. One explanation is that the ridge is too narrow with respect to the spatial resolution of OIB ATM, and thus, only the elevations around the ridge are collected.

Fig. 15(c) shows a similar example. The extracted ridge structure from R_A breaks in the middle of a visually detected ridge L_3 from R_M. There are two saddles along L_3 in the ATM-TIN model, which split L_3 into three parts. The middle part (in the yellow dashed box) between these two saddles is not high enough to be considered as a separate ridge, but the two saddles are low enough to separate it from the two adjacent ridges. Such a ridge line mismatch is common in our results because it is not easy to tell the ridge height change from images, which makes it hard to decide the endpoints of ridge lines. Therefore, when we decided the optimal parameters, we considered mainly the number of matched ridges instead of the total matched length.

3) Statistics of Extracted Ridge Structures: Fig. 16 presents a set of three histograms that describe the ridges extracted from the OIB ATM-TIN using our proposed method, with ω_m = 0.25 m and θ_m = 0.09 m. In the 72-km-long, 26.22 km^2 large study area, a total of 20 558 ridges have been detected. 755 of them do not have ridge lines after the processing, and thus, these are considered to be small features and are excluded from the following statistics. Fig. 16(a) and (b) shows the distributions of ridge lengths and sail elevation anomalies, which are indicators of the overall size of a ridge. Both distributions are right-skewed, with modal values clustered at the lower end of the distribution with a tail extending toward the higher end of the distribution. The modal ridge length is 4.38 m, while the mean length is 25.13 m. Just 1% of ridges

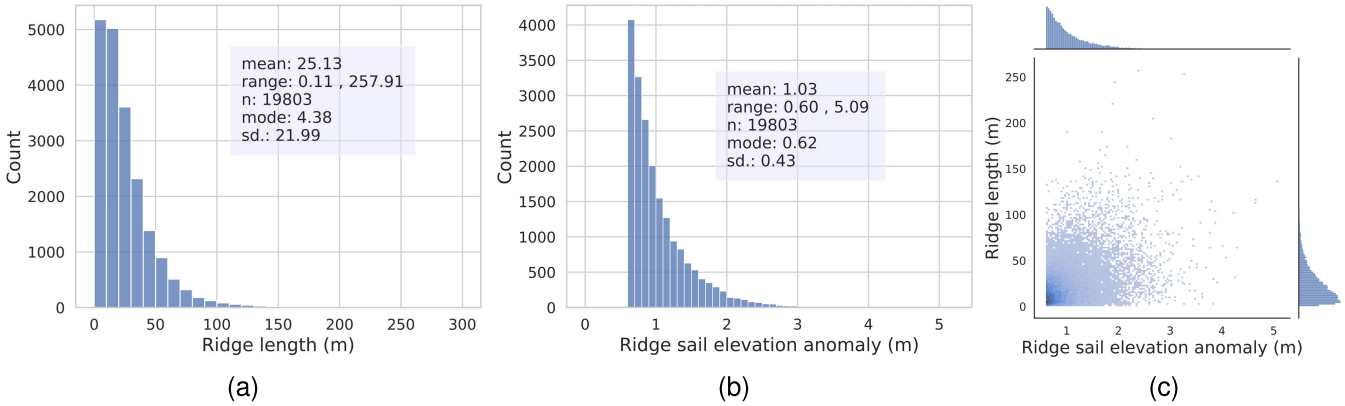

Fig. 16. Statistics of ridge lines in the study area extracted by our method. (a) Ridge length distribution (bin width = 10 m). (b) Ridge sail elevation anomaly H_A distribution (bin width = 0.1 m). (c) Joint distribution of ridge lengths and ridge sail elevation anomalies H_A.

are longer than 106 m. The range of ridge lengths is quite broad, extending from 0.11 to 257.91 m, suggesting a high degree of variability in ridge length measurements. This is further supported by a standard deviation of 21.99 m. Ridge sail elevation anomaly H_A ranges from 0.60 m (the lower height threshold) to 5.09 m, with a small standard deviation of 0.43 m. This might indicate that despite a few taller ridges, most of the ridge sails are clustered around a mean height of 1.03 m. Fig. 16(c) illustrates the joint distribution of ridge length and sail elevation anomaly. It further demonstrates that the sizes of ridges in the study area tend to cluster on the smaller side.

VII. Discussion

In this study, we proposed a new topology-based approach for extracting pressure ridges, which marks a substantial advancement over existing techniques. By analyzing the full 2-D swath, our method yields more detailed information, including range, length, and orientation, which are impossible to be derived from linear scanning results from instruments like ICESat-2. Notably, our method extracts significantly more ridges than independent profile-based or visual inspection methods, suggesting that these traditional profile-based methods and visual-inspection-based approaches may underestimate the true complexity and degree of deformation of the sea ice surface.

The success of this extraction relies on the underlying surface representation using TINs. In contrast to gridded models, TIN-based models preserve the original LiDAR point data without losing information during surface model generation. Many valuable terrain metrics used in terrain analysis, such as slope, curvature, and roughness, can be calculated on TINs efficiently as well [51]. A significant benefit of TIN-based methods is their flexibility in analyzing surface topography at multiple scales. Unlike grid-based methods, where the cell resolution limits the analysis scale, TIN-based methods computing statistics such as surface roughness, use variable search radii, providing more precise and adaptive assessments of elevation statistics. One example of a detailed comparison between roughness fields computed from TIN-based and grid-based surface models is presented in Section S1-C of the Supplementary Material. It shows that the TIN-based method preserves fine-scale topographic variability that is often smoothed out in grid-based methods.

Our preliminary experiments to select roughness radius for the roughness filter show that the roughness distribution is affected by the measuring scales, i.e., the search radii at each vertex. Small features are averaged out when a large scale is used to study sea ice surface topography. In Section S1-B of the Supplementary Material, we put the roughness maps and distributions of all evaluated search radii. These distributions can help guide the design of high-resolution rasterized data products that capture features of interest while also minimizing storage costs. These findings can help scientists decide on suitable resolutions for future altimeters aiming to capture sea ice surface topography at high-resolution. Furthermore, these insights are valuable for simulation models that require accurate representations of the sea ice surface. By examining how roughness distribution varies across different spatial scales, these models can better simulate real-world conditions and phenomena.

Our method to identify regions without LiDAR measurements also provides crucial insights into data quality. In this study, these regions closely correspond to open water regions, consistent with previous findings that, in recent OIB ATM wide-scan datasets [40], data dropouts happen over the water surface [42], [43]. This correlation can guide the detection of features such as melt ponds and leads, which are essential for understanding sea ice dynamics and freeboard measurements. Furthermore, this method can be extended to remove any artifacts introduced by data dropouts, preventing them from deteriorating ridge extraction results.

VIII. Conclusion

This study presented a topology-based workflow for extracting pressure ridges from airborne LiDAR data using TINs. By integrating surface topology constructed based on discrete Morse theory [16] with geometric roughness constraints, we successfully extracted potential ridge lines and their respective elevations. The results show that our method captures

complex ridge orientations missed by 1-D profiles and small-scale features that are often overlooked in visual inspection. The validation against ICESat-2 and optical imagery shows that this study offers a robust automated tool for analyzing sea ice topography. The usage of TINs opens the possibilities for extending from structure lines to precise ranges of deformed ice in the future. Such advancement would facilitate the detailed 3-D modeling of ridges, contributing to the understanding of sea ice morphology and processes.

While our study proves the potential of extracting pressure ridge structures from TIN-based sea ice surface models, we acknowledge the need for further validation with on-site, ground-truth data to confirm these findings. The spatial and temporal ranges of currently available LiDAR swaths are limited as they are mainly collected from airborne altimeters. Future research in sea ice topography stands to benefit from the growing availability of large-scale LiDAR swath data and the application of TIN-based approaches. However, the methods presented here are robust and scalable, particularly when implemented with efficient data structures like Terrain Trees, and are well-positioned to leverage the growing availability of large-scale LiDAR datasets from future missions.

Data and Code Availability

The authors thank the NASA IceBridge instrument and flight teams responsible for collecting and providing the ATM LiDAR data and CAMBOT optical imagery used in this study. These data are available at https:doi.org/10.5067/19SIM5TXKPGT and https://doi.org/10.5067/B0HL940D452L, respectively. They thank the NASA ICESat-2 team for the ATL03 global geolocated photon data, available at https://doi.org/10.5067/ATLAS/ATL03.005. Code used in the creation and analysis of data used in this study is publicly available on GitHub or Zenodo at https://github.com/UMDGeoVis/Terrain_Trees/tree/features/sea_ice_analysis and 10.5281/zenodo.15111030, respectively. The UMD-RDA elevations and ridge locations, ATM elevations, and ATM TIN model data for the 72-km segment used in this study are publicly available on Zenodo at 10.5281/zenodo.15114513

Acknowledgment

The work of Yunting Song was conducted at the Department of Geographical Sciences, University of Maryland, College Park, MD, USA.

References

[1] T. Martin, M. Tsamados, D. Schroeder, and D. L. Feltham, "The impact of variable sea ice roughness on changes in Arctic ocean surface stress: A model study," *J. Geophys. Res., Oceans*, vol. 121, no. 3, pp. 1931–1952, Mar. 2016. [Online]. Available: https://onlinelibrary.wiley.com/doi/abs/10.1002/2015JC011186

[2] G. Castellani, C. Lüpkes, S. Hendricks, and R. Gerdes, "Variability of Arctic sea-ice topography and its impact on the atmospheric surface drag," *J. Geophys. Res., Oceans*, vol. 119, no. 10, pp. 6743–6762, Oct. 2014.

[3] M. Tsamados et al., "Impact of variable atmospheric and oceanic form drag on simulations of Arctic sea ice," *J. Phys. Oceanogr.*, vol. 44, no. 5, pp. 1329–1353, May 2014. [Online]. Available: http://journals.ametsoc.org/doi/10.1175/JPO-D-13-0215.1

[4] D. O. Dammann, H. Eicken, A. R. Mahoney, E. Saiet, F. J. Meyer, and J. C. Craig George, "Traversing sea ice—Linking surface roughness and ice trafficability through SAR polarimetry and interferometry," *IEEE J. Sel. Topics Appl. Earth Observ. Remote Sens.*, vol. 11, no. 2, pp. 416–433, Feb. 2018.

[5] B. A. Lange, J. F. Beckers, J. A. Casey, and C. Haas, "Airborne observations of summer thinning of multiyear sea ice originating from the Lincoln sea," *J. Geophys. Res., Oceans*, vol. 124, no. 1, pp. 243–266, Jan. 2019. [Online]. Available: https://agupubs.onlinelibrary.wiley.com/doi/10.1029/2018JC014383

[6] L. Rabenstein, S. Hendricks, T. Martin, A. Pfaffhuber, and C. Haas, "Thickness and surface-properties of different sea-ice regimes within the Arctic trans polar drift: Data from summers 2001, 2004 and 2007," *J. Geophys. Res., Oceans*, vol. 115, no. C12, p. 2009, Dec. 2010. [Online]. Available: https://agupubs.onlinelibrary.wiley.com/doi/10.1029/2009JC005846

[7] J. C. Comiso, W. N. Meier, and R. Gersten, "Variability and trends in the Arctic sea ice cover: Results from different techniques," *J. Geophys. Res., Oceans*, vol. 122, no. 8, pp. 6883–6900, Aug. 2017. [Online]. Available: https://agupubs.onlinelibrary.wiley.com/doi/10.1002/2017JC012768

[8] T. A. Moon et al., "The Arctic," *Bull. Amer. Meteorological Soc.*, vol. 104, no. 9, pp. S271–S321, Sep. 2023, doi: 10.1175/bams-d-23-0079.1.

[9] T. Markus et al., "The ice, cloud, and land elevation satellite-2 (ICESat-2): Science requirements, concept, and implementation," *Remote Sens. Environ.*, vol. 190, pp. 260–273, Mar. 2017. [Online]. Available: https://linkinghub.elsevier.com/retrieve/pii/S0034425716305089

[10] K. Duncan, S. L. Farrell, L. N. Connor, J. Richter-Menge, J. K. Hutchings, and R. Dominguez, "High-resolution airborne observations of sea-ice pressure ridge sail height," *Ann. Glaciology*, vol. 59, pp. 137–147, Feb. 2018.

[11] W. B. Krabill et al., "Aircraft laser altimetry measurement of elevation changes of the Greenland ice sheet: Technique and accuracy assessment," *J. Geodynamics*, vol. 34, nos. 3–4, pp. 357–376, Oct. 2002. [Online]. Available: https://linkinghub.elsevier.com/retrieve/pii/S0264370702000406

[12] A. A. Petty et al., "Characterizing Arctic sea ice topography using high-resolution IceBridge data," *Cryosphere*, vol. 10, no. 3, pp. 1161–1179, May 2016.

[13] D. Yi, A. Egido, W. H. Smith, L. Connor, C. Buchhaupt, and D. Zhang, "Arctic sea-ice surface elevation distribution from NASA's operation IceBridge ATM data," *Remote Sens.*, vol. 14, no. 13, pp. 1–13, Jul. 2022, doi: 10.3390/rs14133011.

[14] G. Gao, C. Chen, J. Qi, and R. C. Beardsley, "An unstructured-grid, finite-volume sea ice model: Development, validation, and application," *J. Geophys. Res.*, vol. 116, pp. 1–15, Sep. 2011.

[15] T. C. Sutterley, I. Velicogna, X. Fettweis, E. Rignot, B. Noël, and M. van den Broeke, "Evaluation of reconstructions of snow/ice melt in Greenland by regional atmospheric climate models using laser altimetry data," *Geophys. Res. Lett.*, vol. 45, no. 16, pp. 8324–8333, Aug. 2018.

[16] R. Forman, "Morse theory for cell complexes," *Adv. Math.*, vol. 134, no. 1, pp. 90–145, Mar. 1998. [Online]. Available: https://linkinghub.elsevier.com/retrieve/pii/S0001870897916509

[17] M. De Berg, *Computational Geometry: Algorithms and Applications*. Cham, Switzerland: Springer, 2000.

[18] H. Edelsbrunner and E. P. Mücke, "Three-dimensional alpha shapes," *ACM Trans. Graph.*, vol. 13, no. 1, pp. 43–72, Jan. 1994, doi: 10.1145/174462.156635.

[19] M. Studinger and J. Harbeck, "IceBridge CAMBOT L1B geolocated images, version 2," NASA National Snow and Ice Data Center Distributed Active Archive Center Dataset, Boulder, CO, USA, 2019, doi: 10.5067/B0HL940D452L. Accessed: Dec. 2024.

[20] S. Abdalla et al., "Altimetry for the future: Building on 25 years of progress," *Adv. Space Res.*, vol. 68, no. 2, pp. 319–363, 2021.

[21] L. A. Magruder et al., "Monitoring Earth's climate variables with satellite laser altimetry," *Nature Rev. Earth Environ.*, vol. 5, no. 2, pp. 120–136, Jan. 2024, doi: 10.1038/s43017-023-00508-8.

[22] S. Sandven et al., "Sea ice remote sensing—Recent developments in methods and climate data sets," *Surveys Geophys.*, vol. 44, no. 5, pp. 1653–1689, Apr. 2023, doi: 10.1007/s10712-023-09781-0.

[23] B. E. Schutz, H. J. Zwally, C. A. Shuman, D. Hancock, and J. P. DiMarzio, "Overview of the ICESat mission," *Geophys. Res. Lett.*, vol. 32, no. 21, pp. 1–4, Nov. 2005.

[24] R. Kwok, G. F. Cunningham, H. J. Zwally, and D. Yi, "Ice, cloud, and land elevation satellite (ICESat) over Arctic sea ice: Retrieval of freeboard," *J. Geophys. Res., Oceans*, vol. 112, no. C12, pp. 1–19, Dec. 2007.

[25] S. L. Farrell, K. Duncan, E. M. Buckley, J. Richter-Menge, and R. Li, "Mapping sea ice surface topography in high fidelity with ICESat-2," *Geophys. Res. Lett.*, vol. 47, no. 21, pp. 1–9, Nov. 2020, doi: 10.1029/2020GL090708.

[26] J. A. MacGregor, "The scientific legacy of NASA's operation IceBridge," *Rev. Geophys.*, vol. 59, no. 4, Dec. 2021, Art. no. e2021RG000744. [Online]. Available: https://agupubs.onlinelibrary.wiley.com/doi/abs/10.1029/2020RG000712

[27] W. Dierking, O. Lang, and T. Busche, "Sea ice local surface topography from single-pass satellite InSAR measurements: A feasibility study," *Cryosphere*, vol. 11, no. 4, pp. 1967–1985, Aug. 2017.

[28] T. G. Yitayew et al., "Validation of sea-ice topographic heights derived from TanDEM-X interferometric SAR data with results from laser profiler and photogrammetry," *IEEE Trans. Geosci. Remote Sens.*, vol. 56, no. 11, pp. 6504–6520, Nov. 2018.

[29] L. Huang and I. Hajnsek, "A study of sea ice topography in the Weddell and Ross seas using dual-polarimetric TanDEM-X imagery," *Cryosphere*, vol. 18, no. 7, pp. 3117–3140, Jul. 2024.

[30] X. Miao, H. Xie, S. F. Ackley, and S. Zheng, "Object-based Arctic sea ice ridge detection from high-spatial-resolution imagery," *IEEE Geosci. Remote Sens. Lett.*, vol. 13, no. 6, pp. 787–791, Jun. 2016. [Online]. Available: http://ieeexplore.ieee.org/document/7450593/

[31] S. Linow and W. Dierking, "Object-based detection of linear kinematic features in sea ice," *Remote Sens.*, vol. 9, no. 5, p. 493, May 2017. [Online]. Available: http://www.mdpi.com/2072-4292/9/5/493

[32] K. Duncan, S. L. Farrell, J. Hutchings, and J. Richter-Menge, "Late winter observations of sea ice pressure ridge sail height," *IEEE Geosci. Remote Sens. Lett.*, vol. 18, no. 9, pp. 1525–1529, Sep. 2021.

[33] B. Tan, Z.-J. Li, P. Lu, C. Haas, and M. Nicolaus, "Morphology of sea ice pressure ridges in the Northwestern Weddell sea in winter," *J. Geophys. Research: Oceans*, vol. 117, no. C6, pp. 1–13, Jun. 2012.

[34] K. Duncan and S. L. Farrell, "Determining variability in Arctic sea ice pressure ridge topography with ICESat-2," *Geophys. Res. Lett.*, vol. 49, no. 18, Sep. 2022, Art. no. e2022GL100272.

[35] J. F. Beckers, A. H. H. Renner, G. Spreen, S. Gerland, and C. Haas, "Sea-ice surface roughness estimates from airborne laser scanner and laser altimeter observations in fram strait and north of svalbard," *Ann. Glaciology*, vol. 56, no. 69, pp. 235–244, 2015.

[36] R. T. Lowry and P. Wadhams, "On the statistical distribution of pressure ridges in sea ice," *J. Geophys. Res., Oceans*, vol. 84, no. C5, pp. 2487–2494, May 1979. [Online]. Available: https://agupubs.onlinelibrary.wiley.com/doi/10.1029/JC084iC05p02487

[37] P. Soille, *Morphological Image Analysis: Principles and Applications*. Cham, Switzerland: Springer, 1999.

[38] (2024). *Arctic SDI Topographic Basemap. Norwegian Mapping Authority*. [Online]. Available: https://Arctic-sdi.org/services/topografic-basemap/

[39] N. K. Pavlis, S. Kenyon, J. Factor, and S. A. Holmes, "Earth gravitational model 2008," *SEG Technical Program Expanded Abstracts*, vol. 27, no. 1, pp. 761–763, Jan. 2008.

[40] M. Studinger, "IceBridge ATM L1B elevation and return strength, version 2," NASA National Snow and Ice Data Center Distributed Active Archive Center Dataset, Boulder, CO, USA, 2013, doi: 10.5067/19SIM5TXKPGT. Accessed: Dec. 2024.

[41] M. Studinger, "IceBridge narrow swath ATM L1B elevation and return strength, Version 2," NASA National Snow and Ice Data Center Distributed Active Archive Center Dataset, Boulder, CO, USA, 2014, doi: 10.5067/CXEQS8KVIXEI. Accessed: Dec. 2024.

[42] R. Kwok, G. F. Cunningham, S. S. Manizade, and W. B. Krabill, "Arctic sea ice freeboard from IceBridge acquisitions in 2009: Estimates and comparisons with ICESat," *J. Geophys. Res., Oceans*, vol. 117, no. C2, pp. 1–14, Feb. 2012, doi: 10.1029/2011JC007654.

[43] M. Studinger, S. S. Manizade, M. A. Linkswiler, and J. K. Yungel, "High-resolution imaging of supraglacial hydrological features on the Greenland ice sheet with NASA's airborne topographic mapper (ATM) instrument suite," *Cryosphere*, vol. 16, no. 9, pp. 3649–3668, Sep. 2022.

[44] J. Sonntag. (Jun. 2019). *Summer 2019 IceBridge Arctic Flight Plans*. [Online]. Available: https://icebridge.gsfc.nasa.gov/wp-content/uploads/2019/06/flightplans20190625.pdf

[45] T. A. Neumann et al., "ATLAS/ICESat-2 L2A global geolocated photon data, version 5," NASA National Snow and Ice Data Center Distributed Active Archive Center Dataset, Boulder, CO, USA, 2021, doi: 10.5067/ATLAS/ATL03.005. Accessed: Dec. 2024.

[46] V. J. D. Tsai, "Delaunay triangulations in TIN creation: An overview and a linear-time algorithm," *Int. J. Geographical Inf. Syst.*, vol. 7, no. 6, pp. 501–524, Nov. 1993.

[47] M. Teichmann and M. Capps, "Surface reconstruction with anisotropic density-scaled alpha shapes," in *Proc. Visualizat.*, 1998, pp. 67–72.

[48] (2021). *Computational Geometry Algorithms Library (CGAL)*. [Online]. Available: https://www.cgal.org/

[49] A. Paoluzzi, F. Bernardini, C. Cattani, and V. Ferrucci, "Dimension-independent modeling with simplicial complexes," *ACM Trans. Graph.*, vol. 12, no. 1, pp. 56–102, Jan. 1993.

[50] T. Gurung and J. Rossignac, "SOT: A compact representation for tetrahedral meshes," in *Proc. SIAM/ACM Geometric Phys. Model.*, 2009, pp. 79–88.

[51] R. Fellegara, F. Iuricich, Y. Song, and L. D. Floriani, "Terrain trees: A framework for representing, analyzing and visualizing triangulated terrains," *GeoInformatica*, vol. 27, no. 3, pp. 525–564, Jul. 2023. [Online]. Available: https://link.springer.com/10.1007/s10707-022-00472-3

[52] Y. Song, R. Fellegara, F. Iuricich, and L. De Floriani, "Efficient topology-aware simplification of large triangulated terrains," in *Proc. 29th Int. Conf. Adv. Geographic Inf. Syst.*, Beijing, China, Nov. 2021, pp. 576–587, doi: 10.1145/3474717.3484261.

[53] R. Fellegara and Y. Song. (2023). *Terrain Trees Library*. [Online]. Available: https://zenodo.org/records/10714553

[54] A. W. Nolin and E. Mar, "Arctic sea ice surface roughness estimated from multi-angular reflectance satellite imagery," *Remote Sens.*, vol. 11, no. 1, p. 50, Dec. 2018. [Online]. Available: http://www.mdpi.com/2072-4292/11/1/50

[55] T. Johnson, M. Tsamados, J.-P. Müller, and J. Stroeve, "Mapping Arctic sea-ice surface roughness with Multi-angle Imaging SpectroRadiometer," *Remote Sens.*, vol. 14, no. 24, p. 6249, Dec. 2022. [Online]. Available: https://www.mdpi.com/2072-4292/14/24/6249

[56] S. L. Farrell, T. Markus, R. Kwok, and L. Connor, "Laser altimetry sampling strategies over sea ice," *Ann. Glaciology*, vol. 52, no. 57, pp. 69–76, 2011.

[57] U. Fugacci, S. Scaramuccia, F. Iuricich, and L. D. Floriani, "Persistent homology: A step-by-step introduction for newcomers," in *Proc. Italian Chapter Conf.-Smart Tools Apps Comput. Graph.*, 2016, pp. 1–10.

[58] J. W. Milnor, *Morse Theory*. Princeton, NJ, USA: Princeton Univ. Press, 1963.

[59] V. Robins, P. J. Wood, and A. P. Sheppard, "Theory and algorithms for constructing discrete Morse complexes from grayscale digital images," *IEEE Trans. Pattern Anal. Mach. Intell.*, vol. 33, no. 8, pp. 1646–1658, Aug. 2011.

[60] (2024). *Shapely 2.0.3 Documentation*. [Online]. Available: https://shapely.readthedocs.io/en/stable/index.html

[61] (2024). *GeoPandas*. [Online]. Available: https://geopandas.org/en/stable/index.html

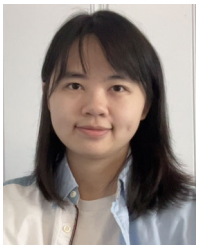

Yunting Song received the bachelor's degree in remote sensing from Wuhan University, Wuhan, China, in 2018, and the Ph.D. degree in geographical sciences from the University of Maryland, College Park, MD, USA, in 2024.

This work was conducted at the University of Maryland. She is currently a Software Engineer at Google, Mountain View, CA 94043 USA. Her research interests include the efficient representation and generation of terrain models, terrain analysis based on hierarchical data structures, and the extension of those algorithms to distributed computing frameworks.

Leila De Floriani (Fellow, IEEE) is currently a Professor with the University of Maryland, College Park, MD, USA. She has previously been a Professor with the University of Genoa, Genoa, Italy. She has also held positions at the University of Nebraska–Lincoln, Lincoln, NE, USA, Rensselaer Polytechnic Institute, Troy, NY, USA, and the Italian National Research Council, Rome, Italy. She has authored over 300 peer-reviewed scientific publications in data visualization, geospatial data representation and processing, computer graphics, geometric modeling, shape analysis and understanding, garnering several best paper awards and invitations as a keynote speaker. Her research has been funded by numerous national and international agencies, including the European Commission and the National Science Foundation.

Ms. Floriani has been a member of the Board of Governors of the IEEE Computer Society (CS) since 2017. She is a fellow of the International Association for Pattern Recognition, a fellow of the Eurographics Association, and a Pioneer of the Solid Modeling Association. She is an IEEE Computer Society Golden Core Member and a member of the IEEE Honor Society IEEE-HKN. She was the Editor-in-Chief of IEEE TRANSACTIONS ON VISUALIZATION AND COMPUTER GRAPHICS from 2015 to 2018. From 2004 to 2008, she served as an Associate Editor for IEEE TRANSACTIONS ON VISUALIZATION AND COMPUTER GRAPHICS. She is the 2020 President of the IEEE Computer Society. She is an Associate Editor of *ACM Transactions on Spatial Algorithms and Systems*, *GeoInformatica*, and *Graphical Models*. She has served on the program committees for over 150 leading international conferences, including several IEEE conferences, and has contributed to many conferences in a leadership capacity.

Kyle Duncan received the B.Sci. degree in physical sciences from the University of Maryland, College Park, MD, USA, in 2011, and the M.Sci. degree in geological sciences from the University at Buffalo, Buffalo, NY, USA, in 2015.

He is currently a Senior Faculty Specialist with the Earth System Science Interdisciplinary Center, University of Maryland. He has served on the NASA/NOAA Ocean Surface Topography and ICESat-2 Science Teams. His research interests include active remote sensing of Earth's polar regions and laser altimetry over sea ice.

Mr. Duncan is a member of the American Geophysical Union and the International Glaciological Society.

Sinéad Louise Farrell received the M.Sci. degree in Earth and space science and the Ph.D. degree in space and climate physics from University College London, London, U.K., in 2002 and 2007, respectively.

She is currently an Associate Professor with the Department of Geographical Sciences and the Department of Atmospheric and Oceanic Science, University of Maryland, College Park, MD, USA. She is also a Principal Investigator on the NASA/NOAA Ocean Surface Topography Science Team and a member of the Mission Advisory Group for the European Copernicus Polar Ice and Snow Topography Altimeter (CRISTAL) mission. She has served on the NASA OIB and ICESat-2 Science Teams. She is also a Visiting Scientist at the NOAA Satellite Oceanography and Climatology Division's Laboratory for Satellite Altimetry and Ocean Topography and Cryosphere Branch. Her research interests include remote sensing of the Earth's polar regions to study cryospheric and oceanic processes.

Dr. Farrell is a member of the American Geophysical Union and the International Glaciological Society.